Atmos. Meas. Tech., 19, 7667–7691, 2026
https://doi.org/10.5194/amt-19-7667-2026
© Author(s) 2026. This work is distributed under
the Creative Commons Attribution 4.0 License.

Atmospheric Measurement Techniques
Open Access
EGU

Radiative Constraints on VIIRS Nighttime Detectability of Lower-Tropospheric Methane

Daja R. Elum[1], Nicholas R. Nalli[2], Johan Villanueva[3], Daniel Yeager[4], Adrian Flores[1], Monique Walker[2], Nakul Karle[1], Ricardo Sakai[1], and Joseph Wilkins[1]

[1]Deparment of Earth, Environment and Equity, Howard University, Washington, DC 20059, USA
[2]National Geospatial-Intelligence Agency, Springfield, VA 22150, USA
[3]Department of Physics, University of Puerto Rico at Mayagüez, Mayagüez, PR 00680, USA
[4]Aerospace Corporation, Chantilly, VA 20151, USA

Correspondence: Daja R. Elum (Daja.elum@bison.howard.edu)

Received: 14 July 2026 – Discussion started: 27 August 2026
Revised: 20 October 2026 – Accepted: 9 November 2026 – Published: 23 November 2026

Abstract. This study investigates the feasibility of detecting nighttime methane (CH_4) plumes in the lower troposphere using operational thermal infrared (TIR) imagery from the VIIRS sensor M12 midwave IR (MWIR) channel (3.7 µm), through a comprehensive radiative transfer sensitivity analysis using MODTRAN6 anchored to a real atmospheric profile. Simulations indicate that the atmosphere in the M12 band is optically thick ($\tau_{\text{eff}} \approx 6.81$) at background methane concentrations, and the detectable signal is therefore driven by the plume's own thermal emission rather than by absorption of surface-emitted radiation. We find that while plumes confined to the shallow nocturnal boundary layer produce a negligible signal regardless of concentration, plumes extending into the deeper residual layer yield substantially larger brightness temperature perturbations. At the native pixel scale, theoretical simulations indicate that detection ($\text{SNR} \geq 2$) is probable only under an extreme high-enhancement scenario at a 9× baseline concentration (∼ 800 % enhancement). Incorporating observationally constrained surface emissivity retrievals from the Combined ASTER and MODIS Emissivity over Land (CAMEL) dataset at 3.6 µm into the uncertainty budget propagated a surface-derived brightness temperature uncertainty of $\sigma_{\text{emis}} = 0.185$ K, exceeding the instrument noise-equivalent temperature difference (NEΔT) and establishing an irreducible noise floor independent of window size. Thus, surface emissivity heterogeneity, rather than instrument noise, dominates detectability, and spatial averaging offers only limited benefit in mixed-covered scenes. Operational nighttime MWIR methane detection would therefore require well-characterized surface emissivity, plumes extending into the residual layer, and, ideally, a narrow band near the 3.3 µm methane feature.

1 Introduction

Satellite measurements of nighttime methane (CH_4) concentrations in the lower troposphere face significant challenges in top-down measurements due to gaps in satellite sensitivity and retrieval capabilities. Within the lower atmosphere, methane concentrations are strongly modulated by the diurnal cycle of the boundary layer (Elum et al., 2026; Tran et al., 2025). During the day, convective mixing leads to a hypothetical uniform profile; however, at night, the formation of a shallow, stable nocturnal boundary layer (NBL) traps emissions, leading to surface accumulation followed by a sharp decrease into the residual layer (RL) and free troposphere above (Botía et al., 2020). Daytime retrievals are typically measured in the shortwave infrared (SWIR) region, because reflected sunlight provides sensitivity across the entire atmospheric column, enabling retrievals of the column-averaged dry-air mole fraction of methane (XCH_4) (Hu et al., 2018; Lorente et al., 2021; Zheng et al., 2026), including from dedicated methane missions such as MethaneSAT (Chan Miller et al., 2024). Nighttime observations must rely on thermal infrared (TIR) energy emitted from Earth's surface and atmosphere. This is accomplished using sensors that operate in the

midwave, longwave, and thermal infrared (MWIR, LWIR, and TIR) regions of the electromagnetic spectrum (Neinavaz et al., 2021; Webber and Kerekes, 2020).

The MWIR region, particularly the 3.0–3.8 µm range, offers the potential for methane detection due to its strong sensitivity to thermal emissions. At these wavelengths, a methane gas plume creates a thermal contrast signal by absorbing upwelling radiation from the surface and emitting at the temperature of the surrounding atmosphere, thereby reducing interference from reflected solar radiation during nighttime observations (Xu et al., 2024). Airborne hyperspectral SEBASS data have been used to detect methane plumes in the MWIR (3–5 µm) and to compare MWIR with LWIR detection (Scafutto and De Souza Filho, 2018). Methane's absorption feature in MWIR is valuable for nighttime TIR analysis because of its strong signal and favourable signal-to-noise ratio (SNR) relative to water vapor, compared to LWIR. The MWIR region serves as an atmospheric window where water vapor absorption is minimal, leading to less uncertainty in retrievals, especially in the lower troposphere, where water vapor is abundant (Lechevallier et al., 2018).

These characteristics highlight MWIR as a promising yet underutilized region for satellite-based nighttime methane retrieval, particularly compared with existing SWIR and LWIR approaches. Previous satellite-based analyses of GOSAT and TROPOMI found near-surface sensitivity in SWIR retrievals, whereas hyperspectral TIR sensors such as CrIS, IASI, and AIRS exhibit higher sensitivity in the mid-upper troposphere (Ni et al., 2023; Xiong et al., 2008; Zhou et al., 2023), but suffer from lower spatial resolution. However, many of these studies have primarily focused on daytime measurements (SWIR) or TIR retrievals in the LWIR range and have not assessed MWIR sensitivity to nighttime enhancements. Consequently, a significant observational gap exists in monitoring near-surface concentrations during nighttime hours, when SWIR sensors cannot operate due to the lack of reflected sunlight. While LWIR sensors can operate at night, their weighting functions typically peak in the mid-troposphere (De Lange and Landgraf, 2018; Siddans et al., 2017), limiting their ability to see emissions trapped in the boundary layer, in addition to interference from water vapor. This necessitates exploring MWIR as a potential solution.

Specifically, the Visible Infrared Imaging Radiometer Suite (VIIRS) M12 (3.61–3.79 µm) band provides an opportunity to explore this phenomenon in the lower troposphere under nighttime conditions. VIIRS, aboard the Suomi NPP, NOAA-20, and NOAA-21 satellites, collects imagery and radiometric data of Earth and atmospheric features across 22 spectral bands ranging from the visible to the infrared spectrum (Hillger et al., 2013). The M12 band is a moderate-resolution Thermal Emissive Band (TEB) designed for high-temperature sensitivity (Cao et al., 2023). Its utility is highlighted in applications such as fire detection and characterization, sea surface temperature, and nighttime cloud detection. For example, the VIIRS Nightfire (VNF) algorithm (Zhizhin et al., 2023) detects and characterizes subpixel infrared radiation from pyrometric methane sources such as burning biomass and natural gas flaring using the M12 and M13 TEBs. However, the success of the VNF algorithm relies on the intense radiance of high-temperature combustion. An unanswered question is whether the M12 band retains sufficient sensitivity to detect the more subtle thermal contrast generated by non-combusted, ambient-temperature methane plumes, and can be distinguished from background noise and other confounding environmental factors.

This research aims to determine the feasibility of detecting non-combusted, ambient-temperature methane plumes using VIIRS M12-band radiance and to quantify the atmospheric and surface conditions under which such detections are possible. To achieve this, we conduct a sensitivity analysis by modelling radiative transfer across a range of methane concentrations in both the NBL and extending to the RL. According to the work of Kaplan (1959, as cited in Menzel, 2001), observations at the wing of an absorbance spectrum permeate deeper into the atmosphere, whereas observations at the absorbance peak are optically deep and only observed from the top of the atmosphere (Menzel, 2001). Based on this, we hypothesize that the M12 band's position on the wing of methane's MWIR absorption feature (cf. Fig. 1) may allow the sensor to detect thermal anomalies from plumes in the lower troposphere.

This study explicitly tests this hypothesis by quantifying the change in at-sensor brightness temperature (ΔBT) resulting from the plume's presence and calculating the corresponding Signal-to-Noise ratio (SNR) relative to both instrument and background noise. Addressing these questions will not only improve our understanding of MWIR sensitivity to methane but also contribute to advancing satellite-based nighttime monitoring capabilities and potentially inform future sensors to include channels better suited for this purpose.

To achieve this, this study utilized the MODerate resolution atmospheric TRANsmission (MODTRAN) 6 model to perform a comprehensive sensitivity analysis of VIIRS M12 nighttime at-sensor radiance. A matrix of simulation ensembles was designed to systematically quantify the influence of three key variables: (1) plume vertical extent (NBL vs. RL); (2) methane concentration (moderate vs. high-enhancement); and (3) surface properties (emissivity from 0.99 to 0.89). The resulting at-sensor radiance and brightness temperature data from these ensembles were then used to quantify detectability and potential measurement biases for each scenario.

2 Methodology

2.1 Radiative Transfer Model and Simulation Setup

Nighttime TIR radiative transfer simulations were performed in MODTRAN6 using the correlated-*k* algorithm to deter-

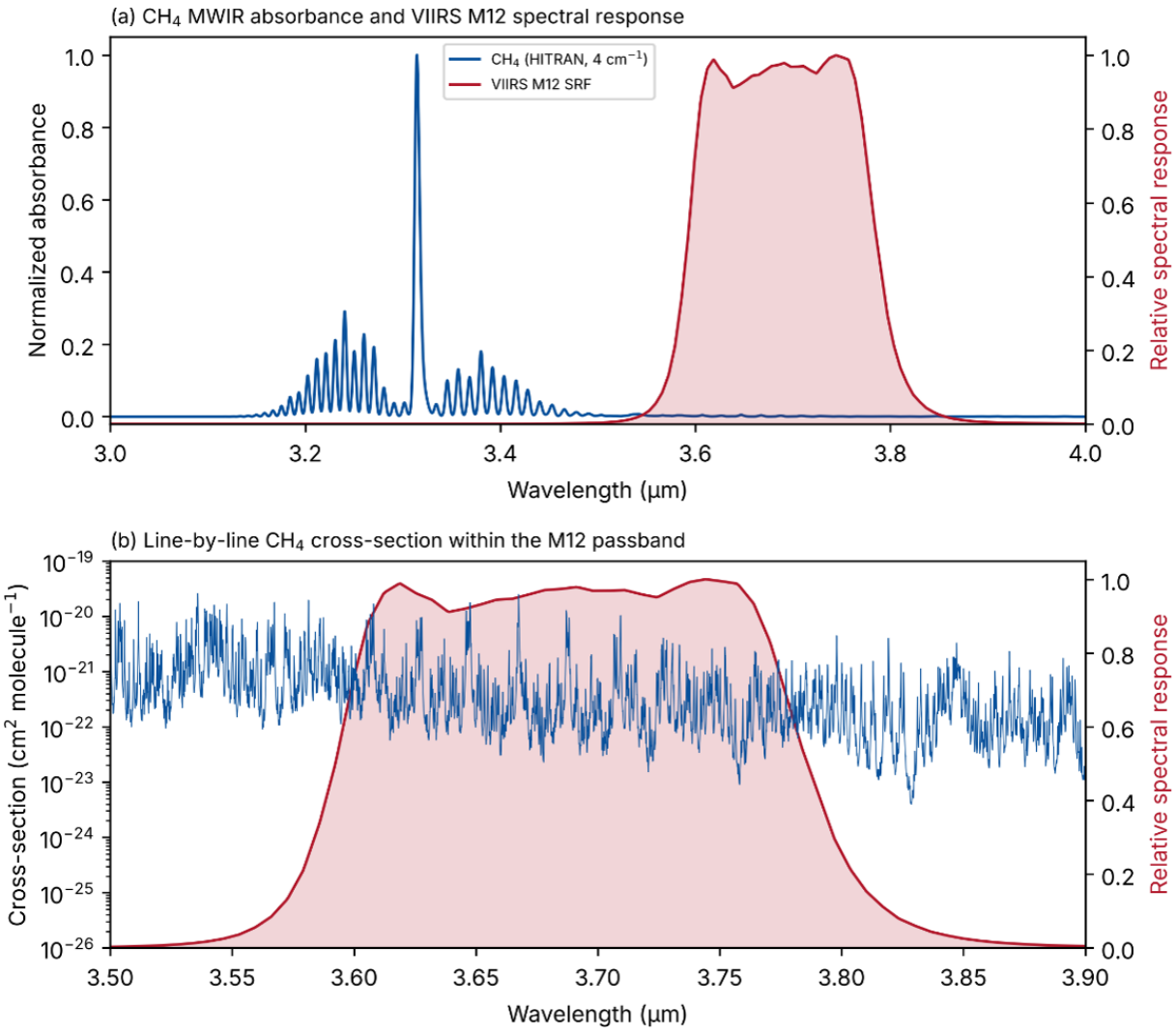

Figure 1. **(a)** Normalized methane absorbance from 3.0 to 4.0 µm, computed from HITRAN2024 line parameters (Gordon et al., 2026) at 296 K and 1 atm. Absorbance is shown in the optically thin limit (proportional to the absorption cross-section), smoothed with a 4 cm^{-1} Gaussian and normalized to its maximum near 3.3 µm. The red curve is the VIIRS M12 relative spectral response. **(b)** Line-by-line methane absorption cross-section from 3.5 to 3.9 µm under the same conditions, with the M12 response. The M12 band (3.61 to 3.79 µm) lies on the long-wavelength wing of the methane MWIR feature, where its response-weighted mean normalized absorbance in **(a)** is about 0.1 % of the maximum.

mine spectral absorption and the Discrete Ordinate Radiative Transfer (DISORT) algorithm to determine radiation propagation through the atmospheric layers. Viewing geometry was set using the VIIRS pixel coincident with the location of Howard University's Beltsville Campus (HUBC) (Lat/Lon ≈ 39.048°, −76.874°) on 19 October 2023, including the satellite zenith angle (5.31°), satellite azimuth (98.27°), and the sensor altitude of 830 km. Figure 2 shows the NOAA-21 VIIRS M12 brightness temperature over the study date for the nighttime overpass. This overpass coincides with a previous campaign at HUBC that assessed surface-level spatiotemporal variability in ambient methane from September 2023 to October 2024. During the 2023–2024 campaign, ground-level, UAV, and radiosonde (RAOB) deployments were conducted to identify diurnal and vertical characteristics of methane concentration in an urban setting (Elum et al., 2026).

Spectral integration was performed using the VIIRS M12 spectral response function (SRF). Accordingly, the simulated spectral window was set to 3500–3930 nm to span the SRF bandwidth. Following MODTRAN6 recommendation to satisfy the CHKRES constraint (runtime warning), a compliant slit-function spectral resolution (full-width, half-maximum, FWHM) and Nyquist-consistent spectral sampling ($\Delta\nu$) were used ($\Delta\nu \leq$ FWHM/2) to ensure adequate sampling of the instrument line shape during SRF-weighted

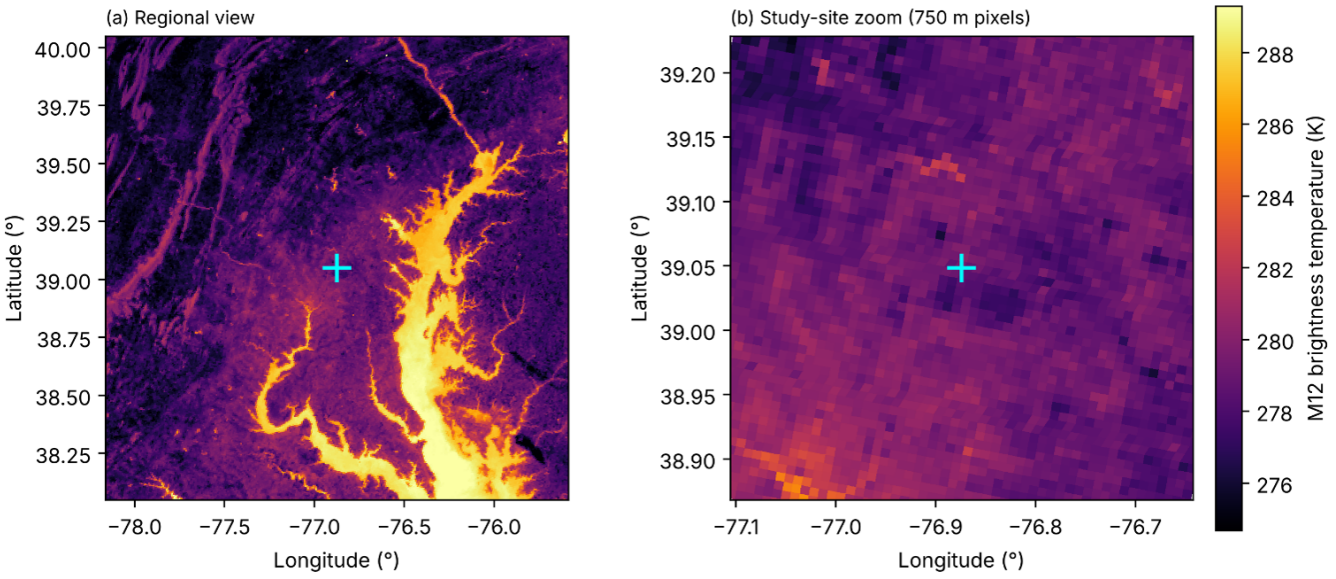

Figure 2. NOAA-21 VIIRS M12 brightness temperature for the nighttime overpass of 19 October 2023 (about 06:56 UTC) at a near-nadir view angle (4.9°). The cross marks the study site. **(a)** Regional view. **(b)** Enlarged view of the study site showing native 750 m pixels. Brightness temperatures were computed from the M12 sensor data record using the standard scale and offset, and the color scale spans the 1st to 99th percentile of the regional view.

integration. Surface-air thermal contrast was prescribed by setting the pixel skin temperature (TPTEMP) to 3 K warmer than the near-surface atmospheric temperature, consistent with TIR plume detection thresholds requiring 3–5 K gradients for realistic plume concentrations (Caico et al., 2017; Webber and Kerekes, 2020). In contrast, the area-averaged boundary temperature (AATEMP) was held at the near-surface value. This modest contrast represents typical nocturnal conditions while enabling measurable BT differences between surface emission and plume absorption/emission.

2.2 Atmospheric Profile Construction

Meteorological inputs (pressure, temperature, and water vapor) were obtained from an RS41-SGP RAOB launched during the VIIRS overpass on 19 October 2023, at HUBC, and used to define a 60-layer MODTRAN6 atmosphere input. The high-resolution data were binned into 60 non-uniform vertical layers: 0.1 km spacing from 0–3 km to capture boundary layer structure, and 0.9 km spacing from 3–30 km for the free troposphere. Within each bin, temperature, pressure, and water vapor were averaged. Water vapor volume mixing ratio (VMR) was derived from the RAOB water vapor mixing ratio (MR) ($g\,kg^{-1}$) using the relation in Eq. (1):

$$\mathrm{VMR} = \frac{\mathrm{MR}}{\epsilon} \times 10^3, \tag{1}$$

Where ϵ is the ratio of the molar masses of water vapor to dry air ($\epsilon = 0.622$). The background methane profile was derived from the Copernicus Atmosphere Monitoring Service (CAMS) global greenhouse gas reanalysis (EGG4) dataset. The 60 methane layers of data were converted from mass mixing ratio ($kg\,kg^{-1}$) to ppmv and interpolated onto the RAOB pressure grid to create a co-registered CH_4−altitude profile, as depicted in Fig. 3.

2.3 Experimental Design: Methane Perturbation Scenarios

To evaluate lower-tropospheric sensitivity in the VIIRS channel, four simulation ensembles were performed across two vertical regimes as seen in Fig. 4. The first regime confined perturbations from the surface to 0.350 km, representing a nocturnal boundary layer (NBL) inferred from the low-level RAOB temperature structure at the time of the VIIRS overpass. This height encompasses the lowest four RAOB levels and represents the shallow, stable layer where nighttime surface emissions are trapped. The second regime extended perturbations through a residual-layer-like (RL) structure from the surface to a ceiling of 1.850 km (the 18th RAOB level), inferred from the broader profile structure. This layer is interpreted as the remnant of the previous day's convective boundary layer, a common scenario for the vertical distribution of pollutants. For each of these two vertical regimes (NBL and RL), the entire CH_4 column within the defined layers was scaled to both a moderate range (0.5–1.5, i.e., ±50 % from baseline) and a high-enhancement range (2–9, i.e., +100 %–800 % enhancement). Layers above the defined ceilings retained the unperturbed CAMS-derived background profile. The resulting CH_4 concentrations in each

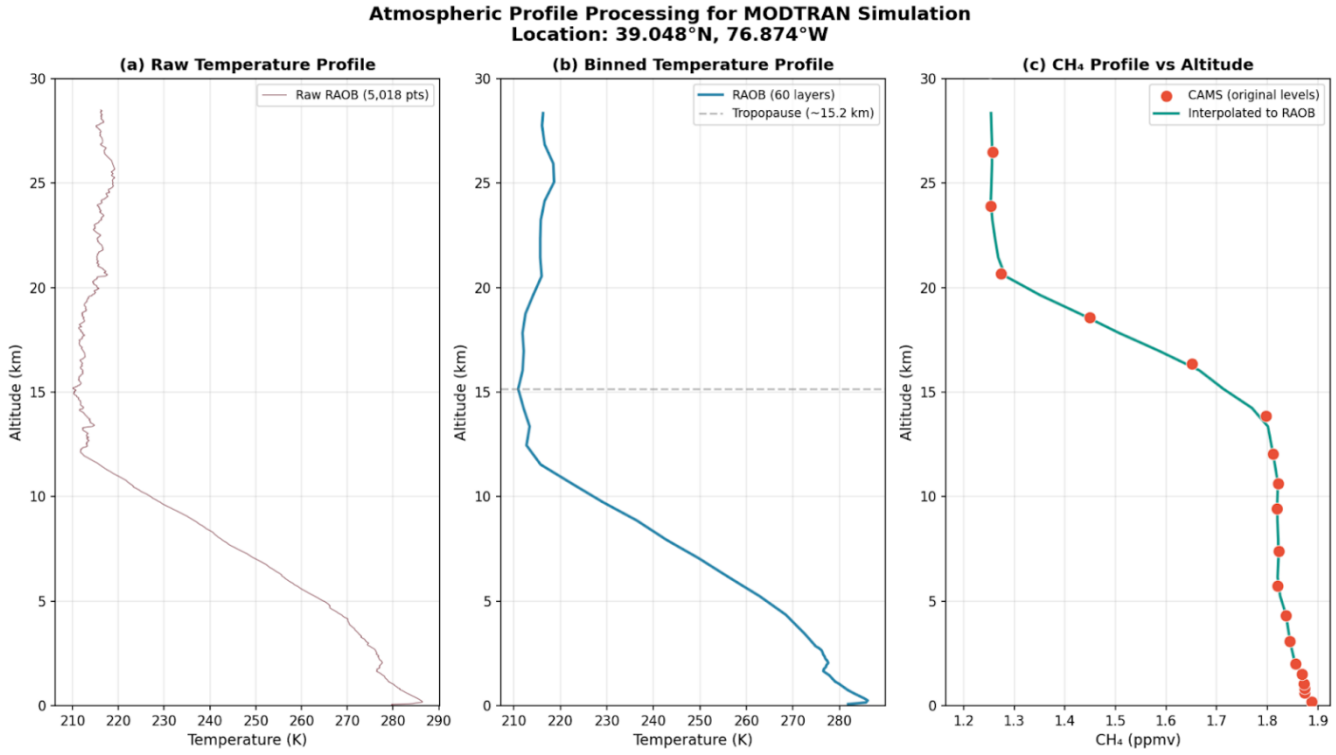

Figure 3. Atmospheric profile construction for MODTRAN6 at HUBC (39.048° N, −76.874° W). **(a)** The raw radiosonde (RAOB) temperature profile (∼ 5000 samples at 1 s resolution) is shown with altitude. **(b)** The RAOB profile binned to 60 non-uniform altitude layers used in MODTRAN: 0.1 km spacing from 0–3 km (30 layers) to resolve boundary-layer structure and 0.9 km spacing from 3–30 km (30 layers) for the free troposphere; within each bin, temperature, pressure, and water vapor were averaged to generate representative layer values. (c) Methane background profile from CAMS (EGG4) converted from mass mixing ratio ($kg\,kg^{-1}$) to ppmv and interpolated onto the RAOB pressure grid, producing a co-registered CH_4–altitude profile for radiative transfer simulations.

model layer across all perturbation scenarios are summarized in Table 1.

The ±50 % moderate perturbation range reflects the realistic variability of boundary-layer CH_4 observed at the HUBC site. During the 2023–2024 campaign, field intercomparison between ground-based analyzers at the site over a two-week deployment yielded ambient concentrations ranging from 2.05 to 2.20 ppm, representing a natural variability of roughly ±7 % around the campaign mean (Elum et al., 2026). The 0.5×–1.5× scaling range deliberately brackets this observed variability, ensuring that the moderate-perturbation regime encompasses both instrument-level uncertainty and the full range of plausible ambient enhancement scenarios above background. Scale factors below 1.0× (depletion scenarios) also characterize the sensitivity floor of the VIIRS M12 sensor by establishing the lower bound of detectable signal change relative to the unperturbed CAMS baseline profile. The 100 %–800 % enhancement range (scale factors 2×–9×) represents idealized high-enhancement sensitivity scenarios, not a direct representation of a specific source-rate threshold. For reference, the EPA defines a methane super-emitter event operationally as a remote-detected source emitting 100 $kg\,h^{-1}$ or more (US Environmental Protection Agency, 2025); no direct conversion of this threshold into a column scaling factor is made here.

2.4 Surface Property Simulation

To account for variability in ground conditions, all simulation ensembles were run across a surface reflectance (ρ) sweep of 0.01–0.11 in the MWIR. For opaque surfaces, this corresponds approximately to a surface emissivity (ϵ) range of 0.99–0.89 using Kirchhoff's approximation ($\epsilon \approx 1-\rho$). Because VIIRS' 750 m pixel integrates a mixture of built and natural land-cover types, the modeled sweep was intended to span plausible effective pixel-scale surface properties rather than represent a single uniform material.

2.5 Data Analysis and Metrics

To determine the radiometric impact of the methane perturbation, we first computed the differential channel brightness temperature (ΔBT). For each simulated case, ΔBT was calculated by subtracting the brightness temperature of the corresponding baseline case (methane scale factor = 1.0) at the

Table 1. Simulated CH_4concentration profiles (ppmv) at the surface, NBL top (0.350 km), and the RL top (1.850 km) for each perturbation scale factor applied within the NBL-only and RL-inclusive regimes at the HUBC site. Baseline (1.0 ×) represents the unperturbed CAMS-derived profile.

Scale Factor	Enhancement (%)	Surface ppmv (NBL)	NBL top ppmv (0.350 km)	RL top ppmv (1.85 km)
0.5	−50 %	0.947	0.9424	0.925
0.6	−40 %	1.1365	1.1309	1.1099
0.7	−30 %	1.3259	1.3194	1.2949
0.8	−19 %	1.5153	1.5078	1.4799
0.9	−9 %	1.7047	1.6963	1.6649
1	+0 %	1.8941	1.8848	1.8499
1.1	+10 %	2.0835	2.0733	2.0349
1.2	+19 %	2.2729	2.2618	2.2199
1.3	+30 %	2.4623	2.4502	2.4049
1.4	+39 %	2.6517	2.6387	2.5899
1.5	+50 %	2.8411	2.8272	2.7749
2	+100 %	3.7882	3.7696	3.6998
3	+200 %	5.6823	5.6544	5.5497
4	+300 %	7.5764	7.5392	7.3996
5	+400 %	9.4705	9.424	9.2495
6	+500 %	11.3646	11.3088	11.0994
7	+600 %	13.2587	13.1936	12.9493
8	+700 %	15.1528	15.0784	14.7992
9	+800 %	17.0469	16.9632	16.6491

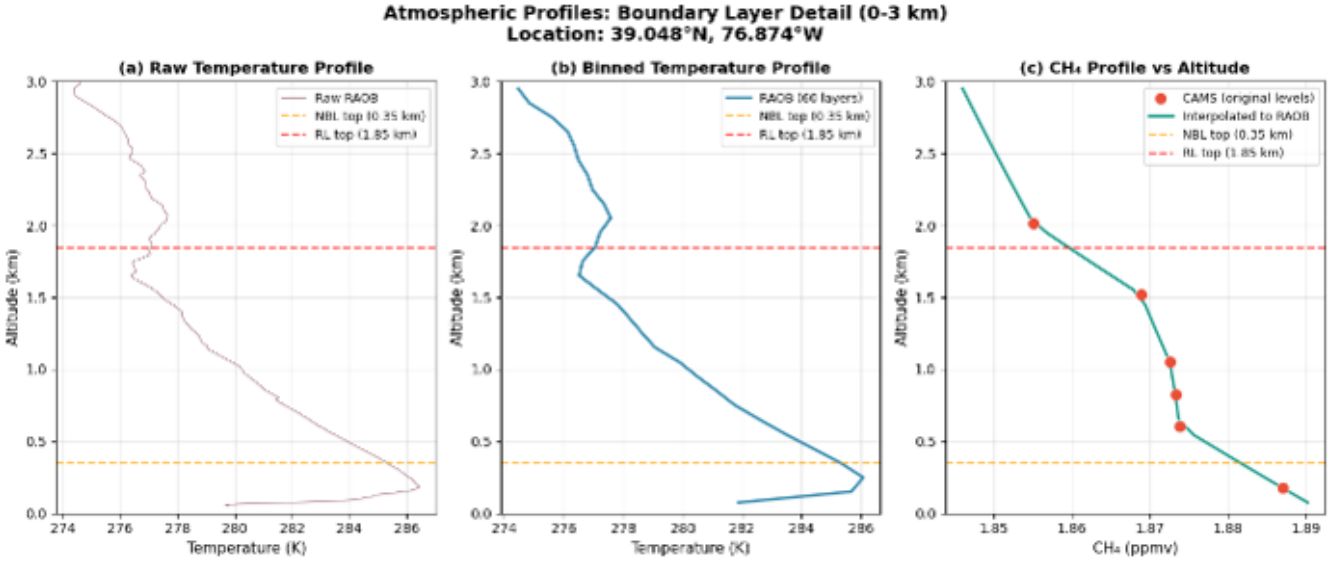

Figure 4. Boundary-layer detail and perturbation layer definitions used to evaluate nighttime lower-tropospheric methane sensitivity. The lower 0–3 km portion of the **(a)** raw and **(b)** binned RAOB temperature profiles and **(c)** the CAMS-derived CH_4 profile are shown with the defined perturbation ceilings. The nocturnal boundary layer (NBL) top was set to 0.350 km to represent nighttime trapping of near-surface emissions during the VIIRS overpass (06:5 UTC/02:54 local time). The residual layer (RL) top was defined at 1.850 km as the remnant of the prior daytime mixed layer. Simulations applied CH_4 perturbations either within the NBL only or across the full nocturnal column, including the RL, to bracket detectability under different vertical distribution scenarios.

same surface emissivity, as shown in Eq. (2):

$$\Delta\mathrm{BT} = \mathrm{BT}(s) - \mathrm{BT}(s = 1.0), \tag{2}$$

Where $\mathrm{BT}(s)$ is the band-averaged brightness temperature for a given methane scale factor(s). Next, to quantify the overall sensitivity of the M12 band to methane changes, we performed an Ordinary Least Squares (OLS) linear regression of brightness temperature against the methane scale factor for each scenario. The sensitivity is defined as the slope of this regression (β_1), as described by the model in Eq. (3):

$$\mathrm{BT}(s) = \beta_0 + \beta_1 s + \epsilon, \tag{3}$$

Where ($\beta_1 \equiv \Delta\mathrm{BT}/\Delta s$) represents the change in brightness temperature per unit change in the methane scale factor (K per unit scale). Finally, to assess detectability, we normalized the absolute value of ΔBT by the published NOAA-21 VIIRS M12 band-averaged noise-equivalent temperature difference (NEΔT) of 0.158 K (Wang et al., 2024) to obtain the SNR for each case by Eq. (4):

$$\mathrm{SNR} = \frac{|\Delta\mathrm{BT}|}{\mathrm{NE}\Delta T}. \tag{4}$$

For this study, we assumed an SNR ≥ 2 as the practical minimum threshold for probable methane detection above instrument noise. We selected M12 over the 375 m imagery band I4 (3.55–3.93 µm) because M12 has lower noise for NOAA-21; at the typical scene temperature of 270 K, the NEΔT for I4 is 0.416 (Wang et al., 2024).

3 Results

3.1 NBL-Confined Plumes

Methane perturbations confined to the NBL, under both moderate (0.5–1.5) and high-enhancement (2–9) scale factors, produce a thermal signal that is overwhelmingly dominated by surface emissivity. As shown in Fig. 5, for the high-enhancement case, the M12 band-equivalent ΔBT increases linearly with CH_4 scaling but remains negligible across all scale factors, with emissivity driving the variation.

Table 2 summarizes and compares the key metrics across the two NBL scenarios. In the moderate case, the maximum ΔBT is only $\pm$0.001 K. While the high-enhancement case is stronger, its maximum ΔBT is 0.011 K, corresponding to a maximum SNR of just 0.070 compared to the NEΔT (0.158 K), which is also an order of magnitude below single-pixel detection thresholds (SNR $\ll 1$).

The OLS regression analysis confirms this observation. The analysis yielded a regression coefficient of 1.5382 for emissivity, compared to 0.0019 for the CH_4 scale factor in the moderate case, confirming that the influence of surface emissivity on the observed BT is stronger than that of the moderate perturbation scenario. Surface emissivity also produced a much larger BT gradient of ~ 0.15 K compared to concentrations alone. Intriguingly, the methane sensitivity coefficient marginally decreases for the high-enhancement (0.0010 vs. 0.0019), suggesting the onset of absorption band saturation. Similar behavior has been reported in TIR methane plume simulations and detection studies, which show that brightness temperature differences quickly become insensitive to further increases in CH_4 enhancement once the effective absorption path is optically thick in the relevant bands (Jongaramrungruang et al., 2021). Although the spectral channel has theoretical sensitivity to the surface layer, there is not enough thermal contrast in the NBL scenario, given the shallowness of the layer and negligible surface-air temperature difference.

3.2 RL Extended Plumes

Because the BT values presented here are derived from MODTRAN6 forward simulation, instrument noise is not included in the modeled signal; detectability is instead evaluated by comparing simulated ΔBT against the VIIRS NEΔT (0.158 K), yielding the SNR metrics reported throughout. Extending methane perturbations into the RL dramatically amplifies the thermal signal. As shown in Fig. 6, ΔBT increases substantially with CH_4 scaling across all emissivities, with individual emissivity values producing a consistent vertical offset. This demonstrates that plume depth is a critical factor for thermal detection, with surface emissivity producing a small spread between emissivity cases relative to the CH_4-driven signal.

Table 3 summarizes the key metrics, confirming that extending the plume into the RL is critical for signal amplification. Under moderate enhancements in the RL, the maximum ΔBT reaches $\pm$0.033 K – a 30-fold increase over the NBL-only case. This is mirrored in the OLS regression, where the methane sensitivity coefficient increased from 0.0019 to 0.0644. In the high-enhancement scenario, extending the plume into the RL produces a detectable thermal signal. The ΔBT reaches $+0.345$ K under the strongest enhancement ($9\times$ scale, $\epsilon = 0.89$). This corresponds to a maximum single-pixel SNR of 2.184 and is the only scenario in our study in which the signal is strong enough to exceed the probable detection threshold of SNR ≥ 2. Furthermore, the data indicate that this threshold is met or exceeded for all enhancements of 800 % ($9\times$ scale) across nearly the entire range of simulated surface emissivities (0.89 to 0.98), confirming that single-pixel detection is feasible under these specific, extreme conditions.

3.3 Optical Depth Analysis

To observe how M12's channel-equivalent BT responds to methane perturbations, how the response differs between boundary layer structures (NBL vs. RL), and methane scaling versus surface emissivity responses, we analyzed the band-

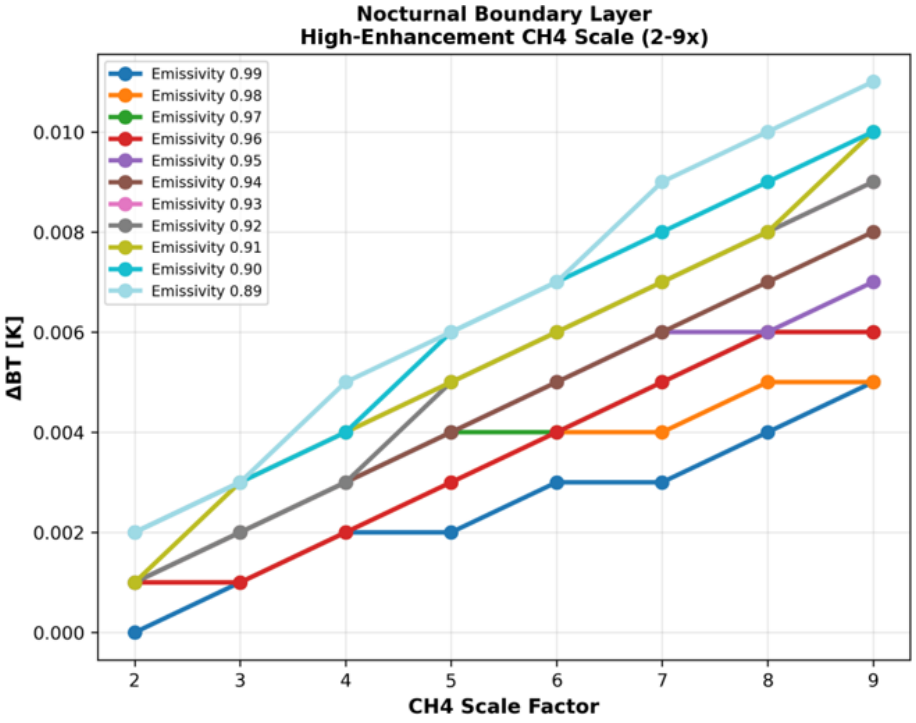

Figure 5. Nocturnal boundary layer (NBL) high-enhancement methane perturbation response in the VIIRS M12 channel shown as brightness temperature anomaly (ΔBT) versus CH_4 scale factor (2–9×; +100 % to +800 %) for surface emissivities ($\epsilon = 0.89$–0.99). ΔBT is computed relative to the baseline methane case (scale facto = 1.0) at each emissivity. ΔBT increases approximately linearly with methane scaling and reaches a maximum of $\sim +0.011$ K under the strongest enhancement.

Table 2. Comparison of summary metrics for VIIRS M12 sensitivity to methane perturbations confined to the Nocturnal Boundary Layer (NBL). Metrics are shown for both a Moderate (0.5–1.5) and a High-enhancement (2–9) concentration range. Reported values include the maximum absolute brightness temperature anomaly (Max $|\Delta$BT$|$) observed across all emissivities, the corresponding maximum Signal-to-Noise Ratio (Max SNR), the approximate average SNR across all cases, and the average sensitivity derived from OLS regression (K per unit scale). The data show that even for a high-enhancement, the maximum SNR remains an order of magnitude below detection thresholds, and the thermal sensitivity decreases with concentration scale, consistent with absorption band saturation.

Methane Scenario	Max Absolute ΔBT (K)	Max SNR	Average SNR	CH_4 Sensitivity (K per scale unit)
Moderate (0.5–1.5×)	0.001	0.006	∼ 0.002	∼ 0.0019
High-enhancement (2–9×)	0.011	0.070	∼ 0.029	∼ 0.0010

effective optical depth (τ_{eff}) and transmittance for each perturbation scenario. Band-effective quantities were computed by integrating the MODTRAN6 channel output over the M12 SRF, following the standard formula for finite-bandwidth radiometers in Eq. (5):

$$\overline{y} = \frac{\int w(v)\, y(v)\, \mathrm{d}v}{\int w(v)\, \mathrm{d}v}, \tag{5}$$

where $y(v)$ is the SRF-weighted mean of a spectral quantity in wavenumber space and $w(v)$ is the NOAA-21 VIIRS SRF. This follows the standard VIIRS band-averaging and SRF convolution approach used in the VIIRS SDR user's guide and in NOAA-21 VIIRS radiometric calibration analyses (Choi et al., 2024). Optical depth was computed from the band-integrated MODTRAN transmittance as $\tau_{\text{eff}} = -\ln(T_{\text{band}})$, and channel brightness temperature was taken directly from the MODTRAN channel-equivalent brightness temperature output. For high-enhancement perturbations, cases were matched to the baseline (1.0 methane scale factor) by emissivity value before differencing.

The baseline band-effective optical depth across all scenarios was $\tau_{\text{eff}} = 6.81$, corresponding to an effective transmittance of approximately 0.0011, indicating that the VIIRS M12 band was largely opaque before and after methane perturbations were applied. Across both moderate (Scale 0.5–1.5) and high-enhancement (Scale 2–9) scenarios, the stan-

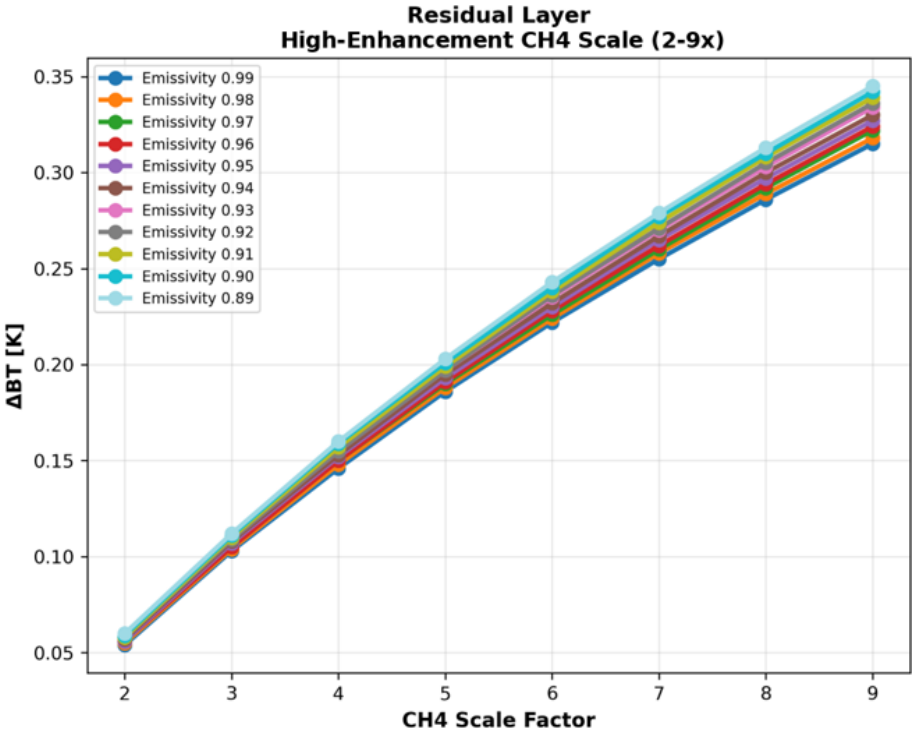

Figure 6. Residual-layer (RL) high-enhancement methane perturbation response in the VIIRS M12 channel shown as brightness temperature anomaly (ΔBT) versus CH_4 scale factor (2–9×; +100 % to +800 %) for surface emissivities ($\epsilon = 0.89$–0.99). ΔBT is computed relative to the baseline methane case (scale factor = 1.0) at each emissivity. ΔBT increases approximately linearly with methane scaling and reaches a maximum of $\sim +0.345$ K under the strongest enhancement.

Table 3. Comparison of summary metrics for VIIRS M12 sensitivity to methane perturbations extending into the Residual Layer (RL). Metrics are shown for both a Moderate (0.5–1.5) and a High-enhancement (2–9) concentration range. The high-enhancement scenario is the only case where the maximum SNR surpasses the detection threshold of 2, indicating a marginally detectable single-pixel signal under extreme conditions.

Methane Scenario	Max Absolute ΔBT (K)	Max SNR	Average SNR	CH_4 Sensitivity (K per scale unit)
Moderate (0.5–1.5×)	0.033	0.228	$\sim$0.111	$\sim$0.0644
High-enhancement (2–9×)	0.345	2.184	$\sim$1.299	$\sim$0.0387

dard deviation of $\Delta\tau$ across the emissivity sweep was zero at all scale factors. This indicates that the M12 band was saturated prior to any methane perturbation, consistent with the diminishing sensitivity coefficients observed in the OLS regression.

3.4 Spatial Averaging

Given that only high-enhancement plumes extending to the RL at 800 % enhancement produced a marginally detectable single-pixel signal, we assessed the feasibility of enhancing this signal through spatial averaging. The framework uses spatial average sampling to first improve the NEΔT from 0.158 K. VIIRS' M12 brightness temperature data were extracted from the HDF5-formatted SDR (Sensor Data Record) file, along with corresponding geolocation information. Raw brightness temperature values were converted to Kelvin using appropriate scaling factors derived from the dataset metadata. To identify the analysis location, we calculated the Euclidean distance from each pixel coordinate to the target location, selecting the pixel with the minimum distance as the center point. We used the nearest pixel to our target coordinates at HUBC to extract a 3×3 window centered on the center pixel, then calculated statistical values such as the mean and standard deviation. We next calculated the spatially averaged NEΔT for N pixels in Eq. (6) as

$$\mathrm{NE}\Delta\mathrm{T}_{\mathrm{eff}} = \frac{\mathrm{NE}\Delta\mathrm{T}}{\sqrt{N}}, \tag{6}$$

where $\mathrm{NE}\Delta T = 0.158$ K and $N = 9$ for the 3×3 window ($\sqrt{9} = 3$). Equation (5) is the standard error of the mean for N measurements with independent, equal random noise (e.g., Bevington and Robinson, 2003), so it applies to random instrument noise only and not to fixed-pattern, calibration, or scene-dependent terms.

Figure 7 shows the histogram of brightness temperatures across the window, with the spatial mean and central pixel overlaid. The distribution indicated relatively low spatial variability within the window. The mean brightness temperature was 279.19 K, while the central pixel value was 279.39 K, yielding a difference of ~ 0.2 K. The standard deviation was 0.46 K, corresponding to a coefficient of variation (CV) of 0.17 %, indicating a thermally homogeneous scene at the scale of the averaging window. The total range across the window was 1.50 K, suggesting modest localized thermal contrast (e.g., surface heterogeneity or sub-pixel variability), but not extreme fragmentation.

Spatial averaging analysis shows that the nominal $\mathrm{NE}\Delta T$ of 0.158 K is reduced to 0.053 K under a 3×3-pixel window. This is consistent with the expected $\sqrt{N}$ reduction in random noise and represents a three-fold improvement in radiometric sensitivity (Eq. 5; Table 4). This averaging increases the effective ground sampling distance from ~ 750 m to ~ 2.25 km. Because the native 750 m footprint is already large relative to a typical point-source plume, averaging also dilutes the plume signal unless the plume fills the averaged footprint, so these gains apply to spatially extensive enhancements. Further expansion to 5×5 and 7×7 windows decreases the effective $\mathrm{NE}\Delta T$ to 0.0316 and 0.0226 K, corresponding to $5\times$ and $7\times$ improvement factors, respectively. However, this instrument-only noise reduction does not fully characterize the detectability limit, as it neglects spatial variability from surface emissivity.

To account for this, we incorporated surface emissivity retrievals from the CAMEL (Combined ASTER and MODIS Emissivity over Land) V002 dataset at 3.6 µm, the closest available wavelength to the VIIRS M12 center wavelength of 3.70 µm. The CAMEL retrieval at the target location yielded a center-pixel emissivity of approximately 0.908. Since the product does not provide per-pixel retrieval uncertainty, the spatial standard deviation of emissivity across a 5×5 window of neighboring pixels (~ 25 km $\times$ 25 km) was used as a proxy for local surface emissivity variability, yielding a standard deviation of 0.0092. This window size was selected to balance spatial proximity to the target location with the need for a sufficient number of pixels to compute a stable standard deviation, given CAMEL's native resolution of $\sim 0.05°$ (~ 5 km). At 3.70 µm and a scene temperature of 279 K, the Planck sensitivity of 20.1 K per unit emissivity propagates this variability into an equivalent BT uncertainty of $\sigma_{\mathrm{emis}} = 0.185$ K. This term represents surface-emissivity heterogeneity and is not assumed to decrease with averaging, as it reflects real scene variation whose spatial covariance at the M12 scale is not resolved by CAMEL (~ 5 km native resolution). The combined uncertainty is computed in quadrature as $\sigma_{\mathrm{combined}} = \sqrt{\mathrm{NE}\Delta T_{\mathrm{eff}}{}^2 + \sigma_{\mathrm{emis}}{}^2}$. For the 3×3 VIIRS window, $\sigma_{\mathrm{combined}} = \sqrt{0.053^2 + 0.185^2} = 0.193$ K. This quantity serves as the operational $\mathrm{NE}\Delta T$, replacing the instrument-only $\mathrm{NE}\Delta T$ of 0.158 K and representing the minimal BT difference detectable under realistic surface conditions at this location. Critically, σ_{emis} dominates this sum, and the instrument noise contribution becomes negligible regardless of window size. Expanding from 3×3 to 7×7 VIIRS pixels reduces $\sigma_{\mathrm{combined}}$ marginally, from 0.193 to 0.187 K, because the emissivity floor remains fixed at 0.185 K across all window sizes. Figure 8 shows the resulting SNR as a function of CH_4 scale factor for both noise floors.

Therefore, no enhancement scenario in our MODTRAN6 simulation set achieved a detectable SNR when compared to the operational $\mathrm{NE}\Delta T$ ($\sigma_{\mathrm{combined}} = 0.193$ K), which incorporates both instrument noise and CAMEL-derived emissivity uncertainty. This represents a direct comparison between the modeled methane signal (ΔBT from MODTRAN6 simulations) and the observationally constrained noise floor ($\sigma_{\mathrm{combined}}$ from CAMEL retrievals). At the CAMEL-matched emissivity of $\epsilon = 0.91$, the maximum simulated ΔBT of 0.339 K ($9\times$ scale factor, RL) yields a combined SNR of only 1.76. Across all emissivity values (0.89–0.99) and all scale factors ($2\times$–$9\times$), the maximum achievable SNR is 1.79, occurring at $\epsilon = 0.89$ and $9\times$ enhancement. Table 4 reflects this revised uncertainty budget, with $\sigma_{\mathrm{combined}}$ remaining effectively constant across window sizes despite $\mathrm{NE}\Delta T_{\mathrm{eff}}$ decreasing by up to $7\times$.

4 Discussion

The simulations in this experiment are theoretical, not observationally validated, and make deliberate assumptions about plume geometry and atmospheric state to isolate radiative roles of plume vertical extent and emissivity. Plumes are treated as horizontally homogeneous within the VIIRS footprint and either entirely confined to the NBL or fully extended to the RL, whereas real plumes exhibit complex three-dimensional structures, shear-induced tilting, and partial pixel filling (Jacob et al., 2016; Worden et al., 2025). Furthermore, the prescribed enhancement factors are radiative sensitivity cases rather than source-rate equivalents, because the pixel-mean enhancement produced by a given emission rate depends on wind, turbulent mixing, source height, plume age, and subpixel coverage. Resolving that relationship would require a coupled plume-dispersion and radiative-transfer framework, which is beyond the scope of this study. Additionally, the radiosonde launch notes indicated partial cloud cover with stratus present in the locale, while the simulations did not explicitly represent clouds. Therefore, the reported sensitivity thresholds should be interpreted most directly as clear-sky idealizations. Likewise, the temperature and water vapor profiles are representative of a mid-latitude

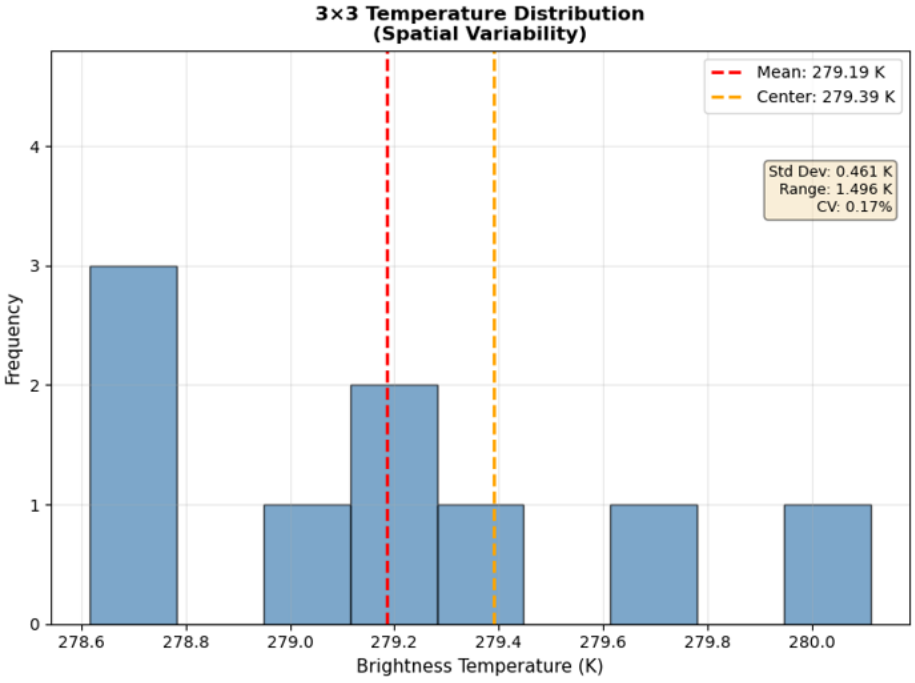

Figure 7. Histogram of VIIRS M12 brightness temperatures within the 3×3 spatial averaging window centered on the M12 pixel nearest to the HUBC RAOB launch site. The red dashed line denotes the spatial mean brightness temperature (279.19 K), and the orange dashed line denotes the central pixel value (279.39 K). The distribution indicates modest spatial variability ($\sigma = 0.46$ K; range = 1.50 K; CV = 0.17 %), with the central pixel slightly warmer than the scene mean (by ~ 0.2 K) but within the overall thermal variability of the window.

Table 4. Effect of spatial averaging window size on brightness temperature statistics and radiometric sensitivity for VIIRS M12 (19 October 2023). Increasing the averaging window from 3×3 (2.25 km) to 7×7 (5.25 km) reduces the effective NEΔT according to $\sqrt{\text{N}}$ scaling, improving theoretical temperature sensitivity by up to $7\times$. However, when surface emissivity heterogeneity is incorporated via CAMEL retrievals at 3.6 µm, using a 5×5 CAMEL pixel sampling window ($\sim 25 \times 25$ km) as a proxy for local emissivity variability, the resulting BT uncertainty of $\sigma_{\text{emis}} = 0.185$ K dominates the combined noise budget. The operational NEΔT (σ_{combined}) remains effectively constant across all VIIRS window sizes (0.193–0.187 K) despite $NE\Delta T_{\text{eff}}$ decreasing from 0.053 to 0.023 K. Larger VIIRS averaging windows also exhibit greater spatial heterogeneity, as reflected in increased standard deviation and brightness temperature range, illustrating the trade-off between radiometric precision and spatial resolution.

Window Size	Pixels	Spatial Res (km)	Mean BT (K)	SD (K)	Range (K)	Original NEΔT (K)	Effective NEΔT (K)	Improvement	σ_{emis} (K) (K)	σ_{combined} (K) (K)
3×3	9	2.25	279.19	0.461	1.50	0.158	0.0527	3.0	0.185	0.193
5×5	25	3.75	279.06	0.599	2.58	0.158	0.0316	5.0	0.185	0.188
7×7	49	5.25	278.85	0.722	4.05	0.158	0.0226	7.0	0.185	0.187

fall condition. In practice, nocturnal inversions and lower-tropospheric moisture vary substantially by synoptic regime, surface type, and season, thereby shifting both the background optical depth and the vertical distribution of thermal contrast. As a result, the specific SNR thresholds and scaling coefficients reported apply to conditions with similar atmospheric conditions, and additional work is needed to map performance across the full range of atmospheric profiles.

Extreme methane releases provide real-world motivation to evaluate conditions for strong-enhancement detectability. For example, the 2015–2016 Aliso Canyon natural-gas storage well blowout in California, the largest recorded natural-gas leak in US history, reached peak emission rates of approximately 60 t CH_4 h^{-1} and released roughly 97 kt of CH_4 over about four months (Conley et al., 2016). Such events show that exceptionally large, sustained releases do occur, though they are extreme cases rather than a global upper bound. The enhancement cases examined here should therefore be interpreted as idealized radiative sensitivity scenarios motivated by extreme-release conditions, not as emission-rate equivalents.

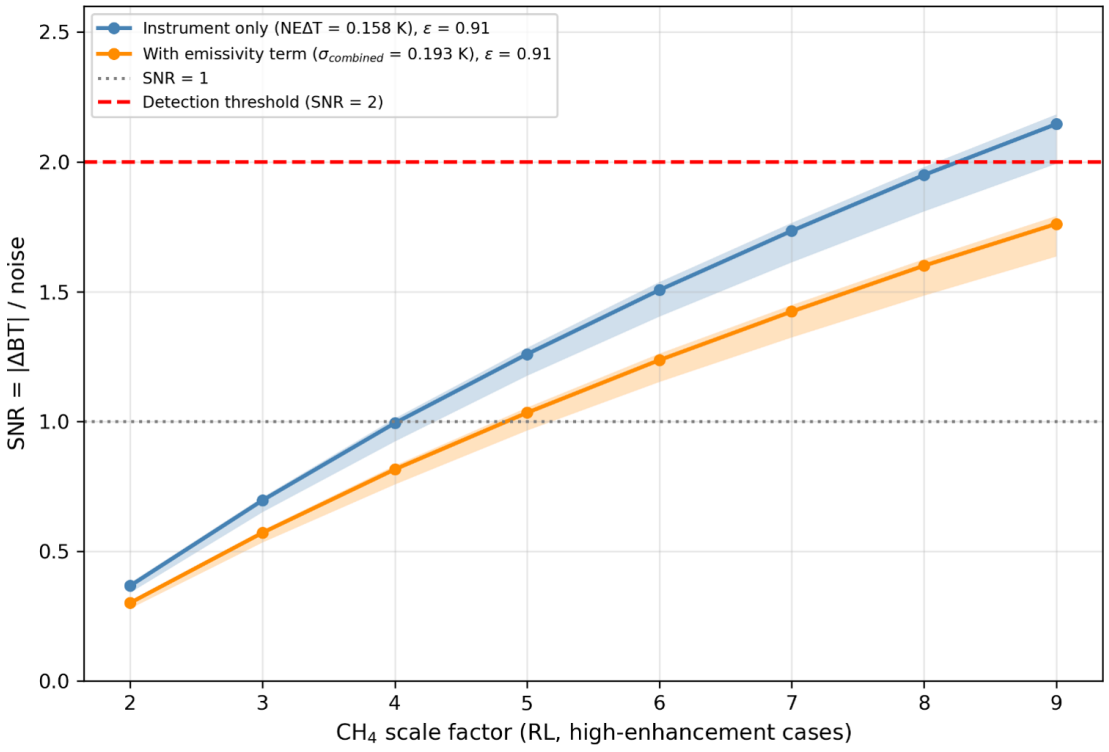

Figure 8. Residual-layer SNR versus CH_4 scale factor (2–9×) for the instrument-only noise floor (NE$\Delta T = 0.158$ K) and the operational noise floor including surface-emissivity variability ($\sigma_{\text{combined}} = 0.193$ K, 3×3 window). Lines show $\epsilon = 0.91$ (CAMEL-matched); shading spans $\epsilon = 0.89$–0.99. The dotted line marks SNR = 1 and the dashed line marks the detection threshold (SNR = 2). With the emissivity term included, no case reaches SNR = 2.

For example, in arid or semi-arid regions, where many major oil and gas basins and associated methane super-emitters are located, low humidity reduces competing water vapor interference, and strong diurnal surface-air temperature cycles can enhance thermal contrast, potentially improving relative methane sensitivity for TIR sensors (Irakulis-Loitxate et al., 2022; Simpson et al., 2024). However, highly heterogeneous surfaces such as bare soil, rock, and sparse vegetation introduce large emissivity-driven BT gradients that our MODTRAN6 simulations show can dominate the M12 signal. We further quantify this operationally with the CAMEL emissivity analysis, where surface heterogeneity alone yields a BT uncertainty of 0.185 K, more than half the maximum simulated methane signal (0.345 K), keeping the combined SNR below the detection threshold across all enhancement levels tested. Over snow and ice, extremely shallow and persistent nocturnal inversions could also confine emissions to layers that are effectively invisible to optically thick TIR channels (Cox et al., 2016; Vihma et al., 2014) unless vertical mixing penetrates the RL. In humid or cloudy boundary layers, additional water vapor and low-cloud emission further increase the scene's optical thickness and reduce sensitivity to near-surface methane, favoring detection only when enhancements extend deeper into the column (Panditharatne et al., 2025; Zhou et al., 2025). Collectively, these regime-dependent behaviors suggest that surface emissivity characterization represents the most critical operational constraint on nighttime MWIR methane detection.

The findings of this study motivate consideration of what sensor modifications or algorithmic approaches would be required for an MWIR instrument to achieve operational nighttime methane detection. Although the VIIRS M12 bandpass was positioned on the tail of methane's primary absorption feature to exploit reduced optical thickness relative to the 3.3 µm peak, our results demonstrate that this spectral positioning alone is insufficient, and the emissivity noise floor dominates the combined uncertainty budget. A purpose-built MWIR methane sensor would likely benefit from a narrow band centered near 3.3 µm to isolate the methane absorption feature from adjacent water vapor interference, paired with high-fidelity surface emissivity characterization to reduce the noise floor this study identifies as the binding detection constraint. Many methane-imaging systems use a dual-filter or dual-band approach, with one channel centered near 3.3 µm for methane absorption and a second comparison channel to support contrast-based detection (Sinfrared and Zimmermann, 2014). Algorithmic approaches such as matched-filter retrievals could further enhance signal isolation, but their effectiveness would still depend on accurate emissivity characterization and stable scene conditions (Roger et al., 2024).

5 Conclusions

Our initial hypothesis was that the VIIRS M12 band, which has a small overlap with the wing of methane's MWIR absorption feature, might detect methane plumes by observing changes in upwelling surface radiance. Our results do not support this mechanism. The observed thermal anomalies therefore are not caused by absorption of surface radiance, but by the sensor detecting thermal emission from the plume itself. Our NBL simulations show that within a strong inversion, even extreme near-surface enhancements produce negligible changes in VIIRS M12 brightness temperature because the additional methane resides in air that is nearly isothermal with the surface and contributes marginally.

A quantitative comparison across four simulated scenarios reveals a clear hierarchy of factors governing the strength of this emission signal. For plumes confined to the NBL, the thermal signal is negligible, with a maximum ΔBT of only $+0.011$ K even for a high enhancement case. In contrast, extending a moderate plume into the RL amplifies its thermal signal to $+0.033$ K. This amplification effect is confirmed by an OLS regression, which shows the sensitivity coefficient for the CH_4 scale factor surging from 0.0019 in the NBL to 0.0644 in the RL – an amplification of over 30 times. This demonstrates that plume depth and thermal contrast are more critical factors for signal strength than near-surface concentration.

However, surface emissivity introduces a critical secondary effect that influences detectability. While higher emissive surfaces produce a warmer absolute brightness temperature, they also create a brighter thermal background that reduces the contrast of the plume's emission signal. Our results consistently show that the methane-driven ΔBT and its corresponding SNR are highest over lower-emissivity surfaces and decrease as emissivity increases. Furthermore, the relationship between concentration and thermal signal is fundamentally non-linear. The regression analysis shows that the sensitivity coefficient for a high-enhancement case in the deep residual layer (0.0387) is notably lower than that of a moderate plume in the same layer (0.0644). This diminishing return provides definitive evidence of gaseous absorption saturation, which limits the potential signal from even the most extreme events.

When spatial averaging is applied to improve instrument sensitivity, an additional operationally critical constraint arises. Incorporating surface emissivity retrievals from the CAMEL dataset at 3.6 µm reveals that real surface heterogeneity at the target location introduces a brightness temperature uncertainty of $\sigma_{\text{emis}} = 0.185$ K, a noise floor that is not reduced by averaging in this analysis and is independent of pixel size. When this emissivity-derived uncertainty is combined with the instrument NEΔT in quadrature, the resulting σ_{combined} of 0.193 K (3×3 window) yields a combined SNR of 1.76 for the maximum simulated methane signal of 0.339 K at the $9\times$ high-enhancement case, which remains below the detection threshold under all window configurations tested. The theoretical improvement from spatial averaging is therefore only realizable over surfaces where emissivity is spatially uniform and retrievable with sufficient accuracy.

Ultimately, this study finds that detection under purely instrument-noise-limited conditions is only marginally feasible for the most extreme high-enhancement scenario: a single-pixel analysis yields a maximum SNR of approximately 2.18 at $9\times$ enhancement (800 %) at $\epsilon = 0.89$. Once real surface emissivity heterogeneity is accounted for operationally, this marginal detectability is eliminated entirely. For an MWIR sensor with similar specifications to become operationally viable for nighttime methane screening, several conditions would need to be satisfied: (1) the target scene would require spectrally uniform, well-characterized, surface emissivity where the noise floor is minimized; (2) the plume would need sufficient vertical extent to penetrate the residual layer; and (3) surface emissivity data of sufficient spatial and spectral resolution would need to be available a priori for uncertainty characterization. Without these conditions, the emissivity noise floor renders the methane signal undetectable, regardless of instrument sensitivity or averaging strategy. Nighttime detectability in the MWIR is therefore governed not only by plume vertical extent and thermal contrast but also by surface emissivity characterization; a constraint that is often overlooked in instrument-noise-limited sensitivity analyses and identified here as the primary barrier to operational methane detection at 3.7 µm.

Appendix A: Figures

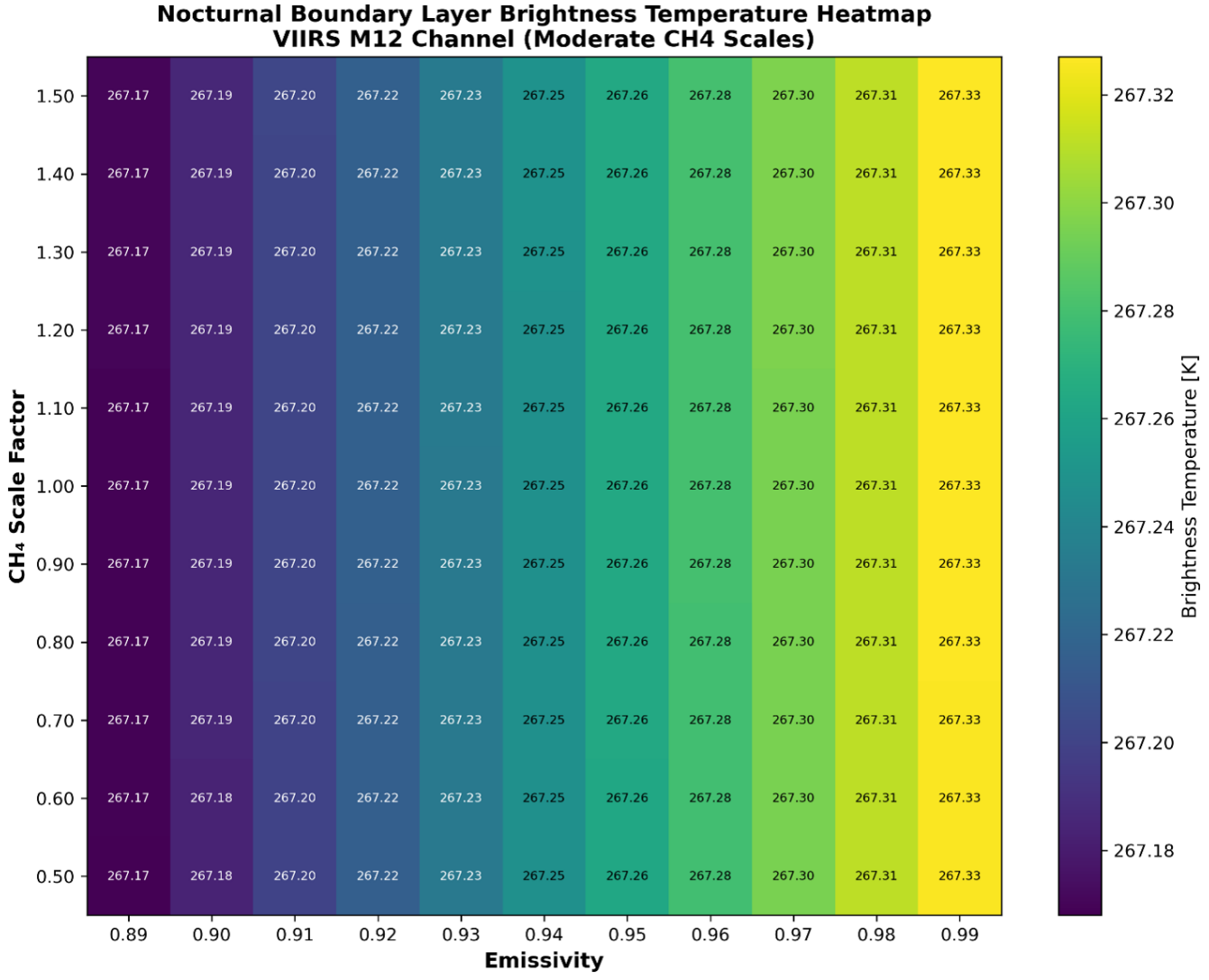

Figure A1. Nocturnal Boundary-layer (NBL) VIIRS M12 band-equivalent brightness temperature (BT) heatmap for moderate methane perturbations (CH_4 scale factor = 0.5–1.5×) shows a strong emissivity-controlled BT gradient (≈ 0.17 K across $\epsilon = 0.89$–0.99), while BT remains nearly invariant with CH_4 scaling (0.5–1.5×), indicating the methane perturbation produces changes at or below the rounding precision ($\sim 10^{-3}$ K). Values annotated in-cell are rounded to 0.01 K; methane-driven ΔBT occurs at ~ 0.001 K scale and is therefore not visually apparent at this rounding.

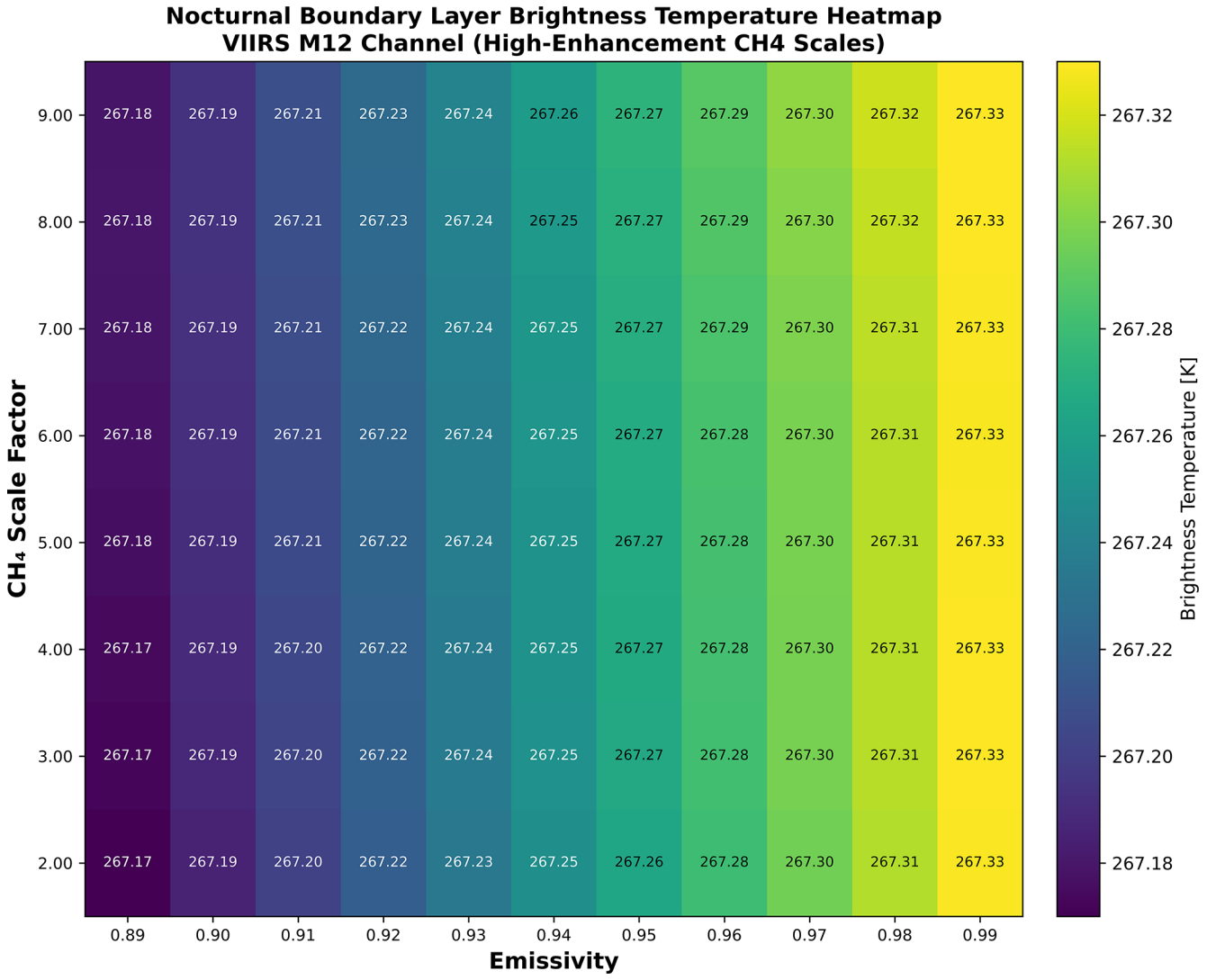

Figure A2. Nocturnal boundary layer (NBL) VIIRS M12 band-equivalent brightness temperature (BT) heatmap for high-enhancement methane perturbations (CH_4 scale factor = 2–9; +100 % to +800 %) under surface emissivities ($\epsilon = 0.89$–0.99). BT values are shown for each emissivity–scale-factor combination. The dominant BT structure is controlled by emissivity (strong horizontal gradient), while methane scaling within the NBL produces only weak within-emissivity BT changes (vertical variation), indicating limited nighttime CH_4 sensitivity for NBL-confined enhancements in M12.

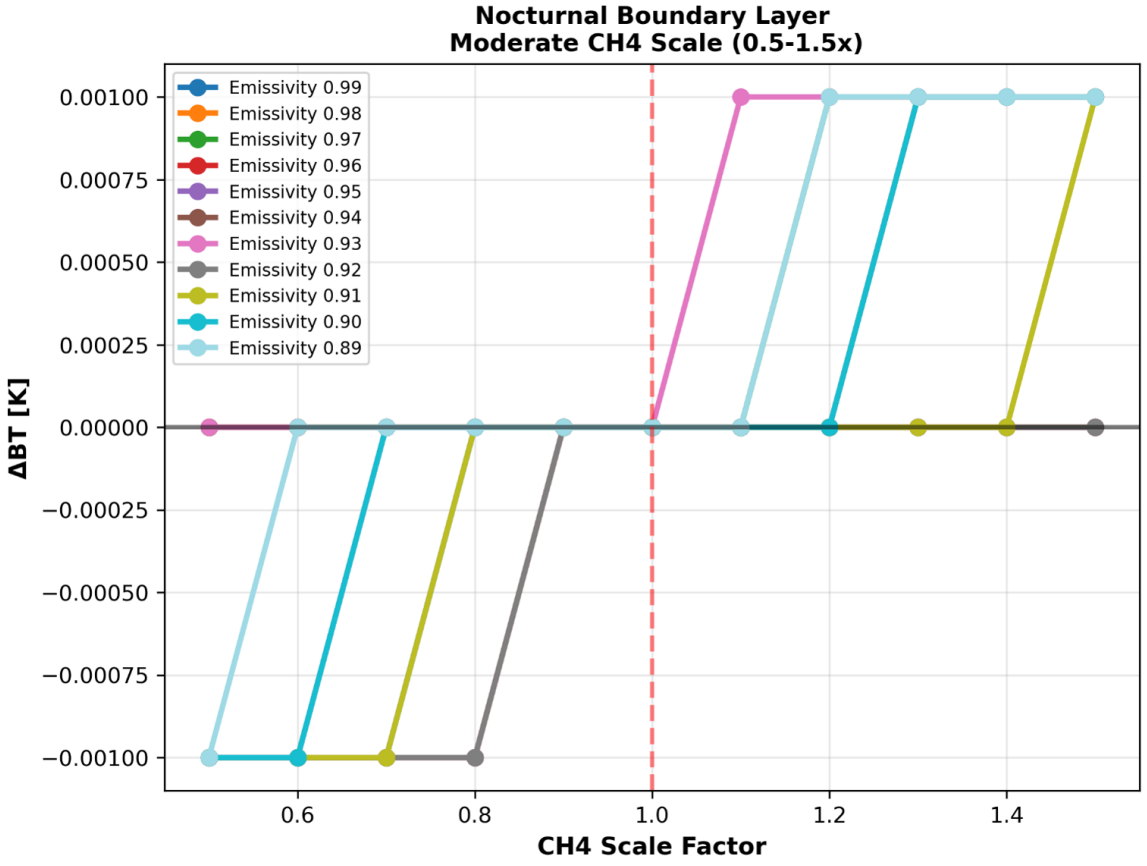

Figure A3. Brightness temperature perturbations (ΔBT) in the VIIRS M12 channel for moderate methane scaling (0.5–1.5×) confined to the nocturnal boundary layer, shown for surface emissivities ($\epsilon = 0.89$–0.99). ΔBT is computed relative to the baseline case (CH_4 scale factor = 1.0; dashed line) at each emissivity. Across all emissivities, ΔBT remains tightly bounded near ± 0.001 K, indicating a radiometrically negligible M12 response to moderate NBL methane variability relative to the instrument noise floor (NE$\Delta T = 0.158$ K).

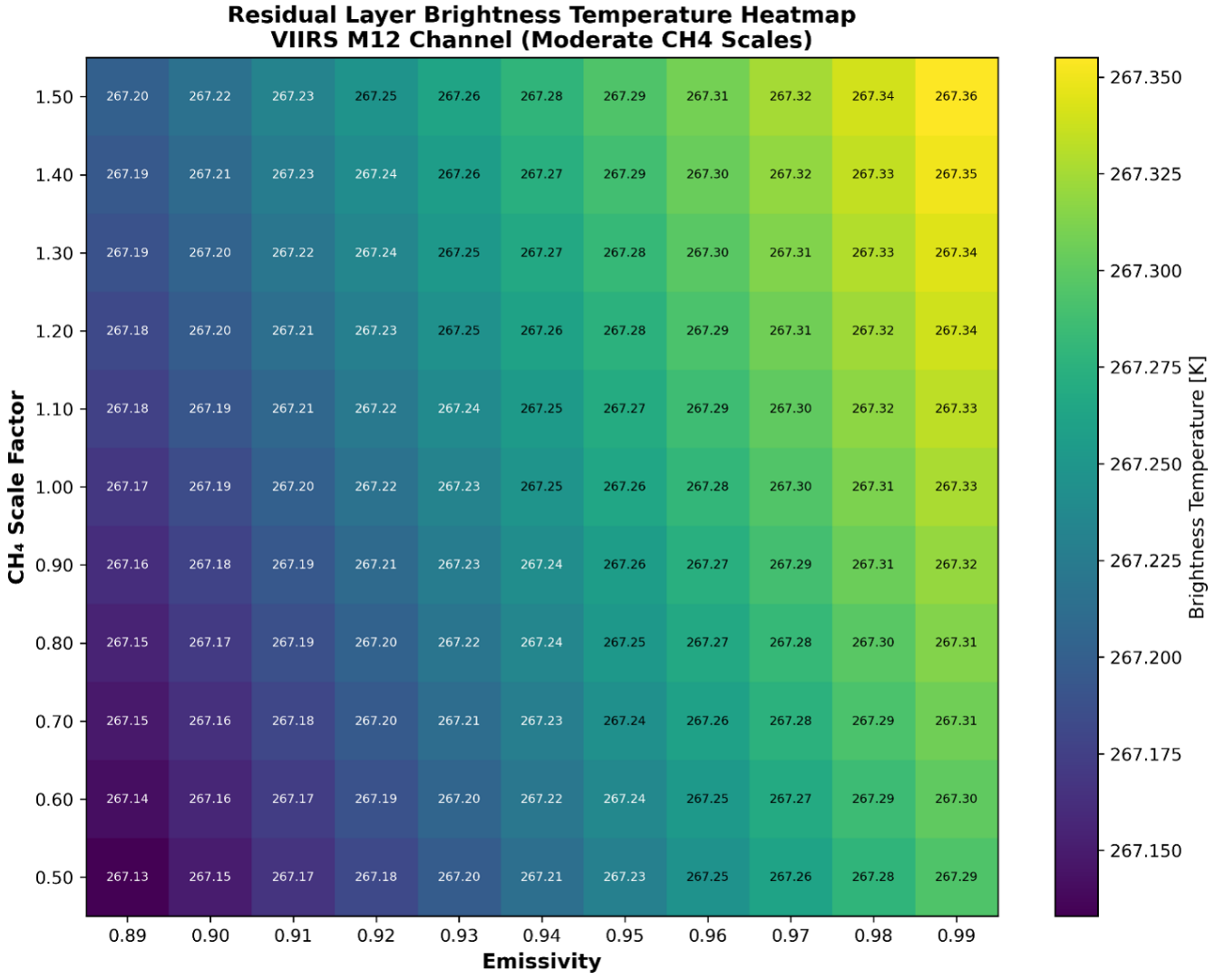

Figure A4. Residual-layer (RL) VIIRS M12 band-equivalent brightness temperature (BT) heatmap for moderate methane perturbations (CH_4 scale factor = 0.5–1.5×) under surface emissivities ($\epsilon = 0.89$–0.99). BT values are shown for each combination of emissivity and CH_4 scaling, illustrating that emissivity primarily controls the absolute BT (strong horizontal gradient), while methane scaling introduces a smaller but coherent BT increase within each emissivity column (vertical gradient) when perturbations extend through the RL.

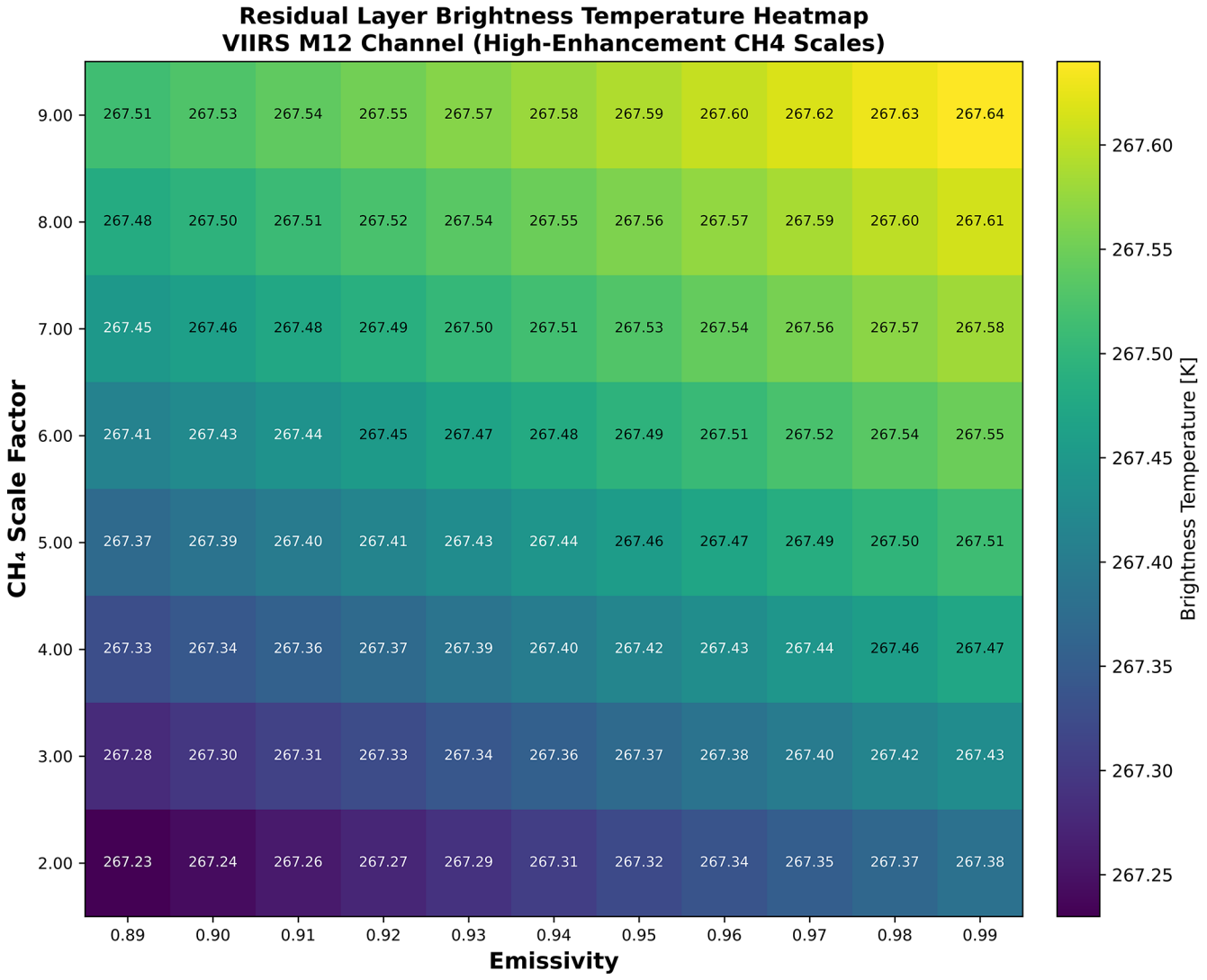

Figure A5. Residual-layer (RL) VIIRS M12 band-equivalent brightness temperature (BT) heatmap for high-enhancement methane enhancements (CH_4 scale factor = 2–9; +100 % to +800 %) under surface emissivities ($\epsilon = 0.89$–0.99). BT values are shown for each emissivity–scale-factor combination. BT increases with methane scaling when enhancements extend through the RL (vertical gradient), while emissivity continues to impose a strong horizontal BT offset across the surface range.

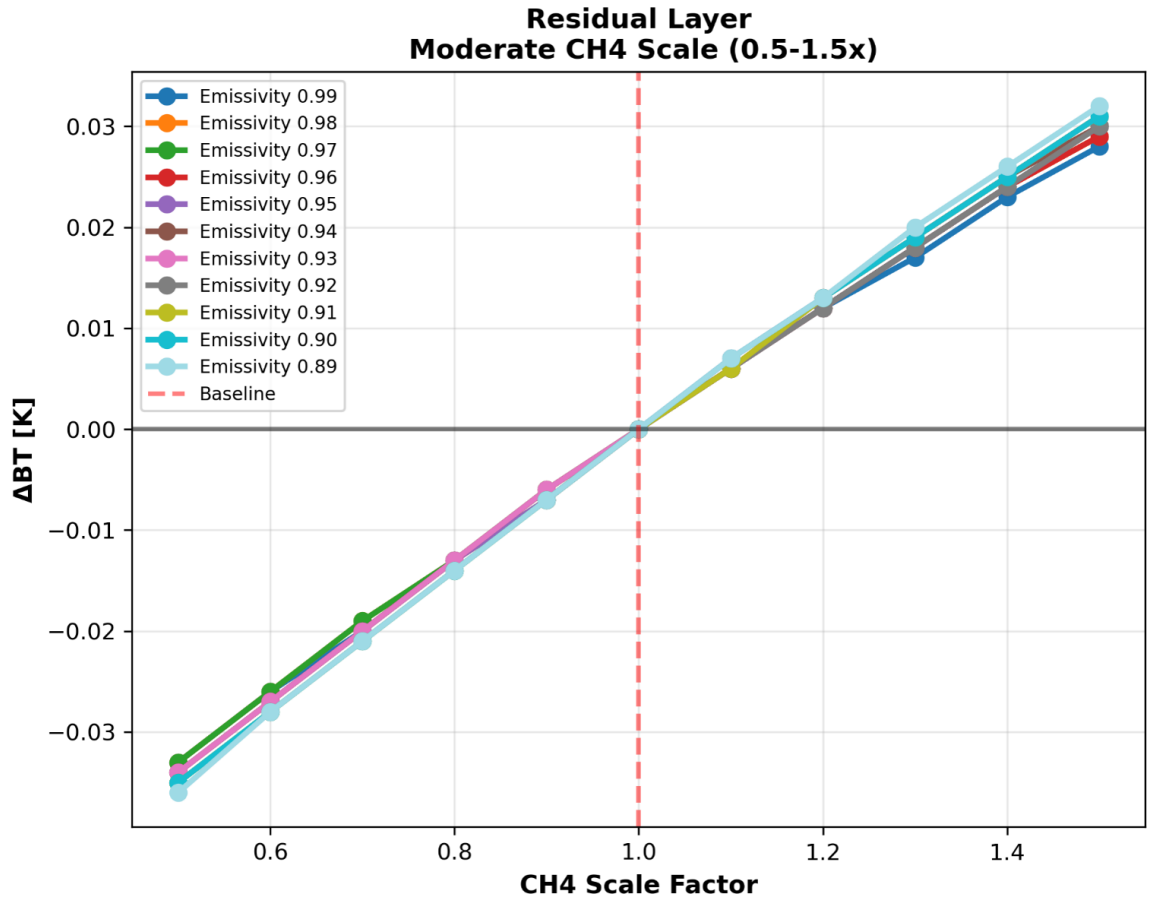

Figure A6. Residual-layer (RL) ΔBT response in the VIIRS M12 channel for moderate methane perturbations (CH_4 scale factor = 0.5–1.5×) under surface emissivities ($\epsilon = 0.89$–0.99). ΔBT is computed relative to the baseline case (scale factor = 1.0; dashed line) at each emissivity. Compared to NBL-only perturbations, RL-inclusive scaling produces a larger and more coherent methane-dependent signal, with ΔBT increasing approximately linearly with CH_4 scale factor and reaching $\sim \pm 0.02$ K across emissivities.

Appendix B: Tables

Table B1. Summary metrics for moderate CH_4 perturbations (0.5–1.5×) confined to the nocturnal boundary layer across surface emissivities ($\epsilon = 0.89$–0.99) in the VIIRS M12 channel. Reported values include the maximum absolute brightness temperature anomaly (max $|\Delta BT|$) relative to the baseline case (scale factor = 1.0), the average signal-to-noise ratio (SNR = $|\Delta BT|/NE\Delta T$; $NE\Delta T = 0.158$ K), and the linear sensitivity of BT to CH_4 scaling (slope of BT vs scale factor; K per unit scale).

Emissivity (ε)	Max Absolute ΔBT (K)	Average SNR	CH_4 Sensitivity (K per scale unit)
0.89	0.001	0.0035	0.0018
0.90	0.001	0.0035	0.0021
0.91	0.001	0.0028	0.0019
0.92	0	0.0023	0.0012
0.93	0.001	0.0029	0.0014
0.94	0.001	0.0017	0.0013
0.95	0	0.0023	0.0013
0.96	0.001	0.0023	0.0013
0.97	0	0.0001	0.0005
0.98	0.001	0.0029	0.0014
0.99	0	0	0

Table B2. Summary detectability metrics for moderate methane perturbations (CH_4 scale factor = 0.5–1.5×) extending through the residual layer (RL) under surface emissivities ($\epsilon = 0.89$–0.99) in the VIIRS M12 channel. Reported values include the maximum absolute brightness temperature anomaly (max $|\Delta BT|$) relative to the baseline case (scale factor = 1.0), the average signal-to-noise ratio (SNR = $|\Delta BT|/NE\Delta T$; $NE\Delta T = 0.158$ K), and the methane sensitivity estimated from the slope of BT versus CH_4 scale factor (K per unit scale).

Emissivity (ε)	Max Absolute ΔBT (K)	Average SNR	CH_4 Sensitivity (K per scale unit)
0.89	0.021	0.0754	0.0437
0.90	0.020	0.0748	0.0434
0.91	0.020	0.0731	0.0425
0.92	0.019	0.0725	0.0409
0.93	0.020	0.0708	0.0413
0.94	0.019	0.0702	0.0408
0.95	0.018	0.0647	0.0398
0.96	0.019	0.0685	0.0396
0.97	0.018	0.0667	0.0387
0.98	0.018	0.0644	0.0375
0.99	0.018	0.0656	0.0379

Table B3. Nocturnal boundary layer (NBL) ΔBT response in the VIIRS M12 channel for high-enhancement methane perturbations (CH_4 scale factor = 2–9×; +100 % to +800 %) across surface emissivities ($\epsilon = 0.89$–0.99). ΔBT is computed relative to the baseline case (scale factor = 1.0) at each emissivity. ΔBT increases monotonically with CH_4 scaling but remains ≤ 0.012 K, and the methane-driven signal weakens as emissivity increases (e.g., maximum ΔBT decreases from ~ 0.012 K at $\epsilon = 0.89$ to ~ 0.005 K at $\epsilon = 0.99$).

Emissivity (ε)	Max Absolute ΔBT (K)	Average SNR	CH_4 Sensitivity (K per scale unit)
0.89	0.012	0.0468	0.0014
0.90	0.011	0.0419	0.0013
0.91	0.011	0.0387	0.0013
0.92	0.01	0.0340	0.0012
0.93	0.01	0.0340	0.0012
0.94	0.009	0.0372	0.0011
0.95	0.008	0.0285	0.0010
0.96	0.008	0.0285	0.0010
0.97	0.007	0.0245	0.0001
0.98	0.007	0.0253	0.0001
0.99	0.005	0.0198	0.0001

Table B4. Summary metrics for residual-layer (0–1.85 km) high-enhancement methane enhancements (CH_4 scale factor 2–9×) across surface emissivities ($\epsilon = 0.89$–0.99). For each emissivity, the maximum absolute ΔBT, corresponding maximum SNR ($\max|\Delta BT|/NE\Delta T$; $NE\Delta T = 0.158$ K), and methane sensitivity (slope of ΔBT versus CH_4 scale factor) are reported.

Emissivity (ε)	Max Absolute ΔBT (K)	Max SNR	CH_4 Sensitivity (K per scale unit)
0.89	0.345	2.1835	0.0404
0.90	0.342	2.1646	0.0401
0.91	0.339	2.1456	0.0398
0.92	0.336	2.1266	0.0394
0.93	0.334	2.1139	0.0391
0.94	0.330	2.0886	0.0387
0.95	0.327	2.0696	0.0387
0.96	0.324	2.0506	0.0380
0.97	0.322	2.0380	0.0377
0.98	0.318	2.0127	0.3729
0.99	0.315	1.9937	0.0369

Appendix C: OLS Regression Results

Table C1. Ordinary Least Squares Regression analysis results for moderate perturbations in the nocturnal boundary layer.

Components	Coefficient	SD	t	$p > \|t\|$	0.025	0.975
Intercept	265.7669	0.001	3.06e+05	0.000	265.765	265.769
Emissivity	1.5745	0.001	1714.467	0.000	1.573	1.576
Scale Factor	0.0012	9.18e−05	13.229	0.000	0.001	0.001

Table C2. Ordinary Least Squares Regression analysis results for high-enhancement perturbations in the nocturnal boundary layer.

Components	Coefficient	SD	t	$p > \|t\|$	0.025	0.975
Intercept	265.8015	0.002	1.39e+05	0.000	265.798	265.805
Emissivity	1.5382	0.002	759.453	0.000	1.534	1.542
Scale Factor	0.0010	2.8e−05	34.342	0.000	0.001	0.001

Table C3. Ordinary Least Squares Regression analysis results for moderate perturbations in the residual layer.

Components	Coefficient	SD	t	$p > \|t\|$	0.025	0.975
Intercept	265.7014	0.003	1.01e+05	0.000	265.696	265.707
Emissivity	1.5760	0.003	569.203	0.000	1.570	1.581
Scale Factor	0.0644	0.000	232.469	0.000	0.064	0.065

Table C4. Ordinary Least Squares Regression analysis results for high-enhancement perturbations in the residual layer.

Components	Coefficient	SD	t	$p > \|t\|$	0.025	0.975
Intercept	265.9288	0.026	1.02e+04	0.000	265.877	265.980
Emissivity	1.3952	0.028	50.652	0.000	1.340	1.450
Scale Factor	0.0387	0.000	101.853	0.000	0.038	0.039

Data availability. VIIRS M12 (3.7 µm) Level-1B calibrated radiances were obtained from the VNP02MOD product, Collection 2 (Lin et al., 2022; https://doi.org/10.3390/rs14174212), distributed via NASA LAADS DAAC (Lin et al., 2022). Viewing geometry was obtained from the corresponding NOAA-21 (JPSS-2) GMODO geolocation granule, distributed via the NOAA Comprehensive Large Array-data Stewardship System (CLASS) (Cao et al., 2012). The VIIRS M12 relative spectral response function used in MODTRAN6 simulations was obtained from the NOAA National Calibration Center (CAO et al.. 2023). Atmospheric methane profiles used to configure MODTRAN6 simulations were derived from the CAMS global greenhouse gas reanalysis (EGG4), produced by ECMWF and distributed via the Copernicus Atmosphere Data Store (Copernicus Atmosphere Monitoring Service, 2021; https://doi.org/10.24381/cda4ed31). Radiosonde profile measurements were obtained from the Howard University Beltsville Campus (HUBC) station of the GCOS Reference Upper-Air Network (GRUAN). MODTRAN6 (Spectral Sciences, Inc.) is proprietary radiative transfer software licensed on a commercial basis and is not publicly redistributable (Berk et al., 2014).

Author contributions. Formal analysis, investigation, writing – original draft preparation, and visualization DRE. Conceptualization, NN. MODTRAN modelling configuration and assistance, JV and DY. Radiosonde data deployment, AF. Project Administration, MW. Writing – review and editing, RS, NK, and JW. All authors have read and agreed to the published version of the manuscript.

Competing interests. The contact author has declared that none of the authors has any competing interests.

Disclaimer. Publisher's note: Copernicus Publications remains neutral with regard to jurisdictional claims made in the text, published maps, institutional affiliations, or any other geographical representation in this paper. The authors bear the ultimate responsibility for providing appropriate place names. Views expressed in the text are those of the authors and do not necessarily reflect the views of the publisher.

Acknowledgements. The authors thank the National Geospatial-Intelligence Agency (NGA) and Howard University (HU) Cooperative Research and Development Agreement XHM0476CRFY20001, Application of Remote Sensing for GEOINT, for providing technical assistance.

Financial support. This research has been supported by the US Department of Energy (grant no. DE-SC0024489), the National Aeronautics and Space Administration (grant no. 80NSSC21K0435), and the National Oceanic and Atmospheric Administration (grant no. NA22SEC4810015).

Review statement. This paper was edited by Daniel Varon and reviewed by two anonymous referees.

References

Berk, A., Conforti, P., Kennett, R., Perkins, T., Hawes, F., and Van Den Bosch, J.: MODTRAN6: a major upgrade of the MODTRAN radiative transfer code, SPIE Defense + Security, 90880H, https://doi.org/10.1117/12.2050433, 2014.

Bevington, P. R. and Robinson, D. K.: Data reduction and error analysis for the physical sciences, 3rd ed., McGraw-Hill, Boston, 320 pp., https://catalogue.library.cern/literature/y1nv4-yfv90 (last access: 8 October 2026), 2003.

Botía, S., Gerbig, C., Marshall, J., Lavric, J. V., Walter, D., Pöhlker, C., Holanda, B., Fisch, G., de Araújo, A. C., Sá, M. O., Teixeira, P. R., Resende, A. F., Dias-Junior, C. Q., van Asperen, H., Oliveira, P. S., Stefanello, M., and Acevedo, O. C.: Understanding nighttime methane signals at the Amazon Tall Tower Observatory (ATTO), Atmos. Chem. Phys., 20, 6583–6606, https://doi.org/10.5194/acp-20-6583-2020, 2020.

Caico, C., Fragu, L., and Gonzalez, L.: An evaluation of an optical gas imaging system for the quantification of fugitive hydrocarbon emissions, Concawe, Brussels, 1 p., https://www.concawe.eu/publication/ (last access: 18 March 2026), 2017.

Cao, C., Deluccia, F., Qiu, S., and NOAA Joint Polar Satellite System Program Office: NOAA JPSS Visible Infrared Imaging Radiometer Suite (VIIRS) Sensor Data Record (SDR) from IDPS, NCEI [data set], https://doi.org/10.7289/V58G8HSZ, 2012.

Cao, C., Xiong, J., Wolfe, R., DeLuccia, F., Liu, Q., Blonski, S., Lin, G., Nishihama, M., Pogorzala, D., and Oudrari, H.: Visible/Infrared Imager Radiometer Suite (VIIRS) Sensor Data Record (SDR) User's Guide, 1.1, NOAA/NESDIS/STAR, College Park, MD 20740, https://ncc.nesdis.noaa.gov/VIIRS/UsersGuide.php (last access: 14 March 2026), 2023.

Chan Miller, C., Roche, S., Wilzewski, J. S., Liu, X., Chance, K., Souri, A. H., Conway, E., Luo, B., Samra, J., Hawthorne, J., Sun, K., Staebell, C., Chulakadabba, A., Sargent, M., Benmergui, J. S., Franklin, J. E., Daube, B. C., Li, Y., Laughner, J. L., Baier, B. C., Gautam, R., Omara, M., and Wofsy, S. C.: Methane retrieval from MethaneAIR using the CO_2 proxy approach: a demonstration for the upcoming MethaneSAT mission, Atmos. Meas. Tech., 17, 5429–5454, https://doi.org/10.5194/amt-17-5429-2024, 2024.

Choi, T., Cao, C., Blonski, S., Shao, X., Wang, W., and Ahmad, K.: Preliminary Assessment of On-Orbit Radiometric Calibration Challenges in NOAA-21 VIIRS Reflective Solar Bands (RSBs), Remote Sens., 16, 2737, https://doi.org/10.3390/rs16152737, 2024.

Conley, S., Franco, G., Faloona, I., Blake, D. R., Peischl, J., and Ryerson, T. B.: Methane emissions from the 2015 Aliso Canyon blowout in Los Angeles, CA, Science, 351, 1317–1320, https://doi.org/10.1126/science.aaf2348, 2016.

Copernicus Atmosphere Monitoring Service (2021): CAMS global greenhouse gas reanalysis (EGG4), Copernicus Atmosphere Monitoring Service (CAMS) Atmosphere Data Store [data set], https://doi.org/10.24381/cda4ed31, 2021.

Cox, C. J., Rowe, P. M., Neshyba, S. P., and Walden, V. P.: A synthetic data set of high-spectral-resolution infrared spectra for the Arctic atmosphere, Earth Syst. Sci. Data, 8, 199–211, https://doi.org/10.5194/essd-8-199-2016, 2016.

De Lange, A. and Landgraf, J.: Methane profiles from GOSAT thermal infrared spectra, Atmos. Meas. Tech., 11, 3815–3828, https://doi.org/10.5194/amt-11-3815-2018, 2018.

Elum, D., Karle, N. N., Sakai, R. K., Ren, X., Stratton, P., Nalli, N. R., Walker, M., Flores, A., Villanueva, J. R., and Wilkins, J.: High Resolution UAV-Based Monitoring of Ambient Methane: Field Deployment and Intercomparison with Reference Standards, Remote Sens., 18, 549, https://doi.org/10.3390/rs18040549, 2026.

Gordon, I. E., Rothman, L. S., Hargreaves, R. J., Gomez, F. M., Bertin, T., Hill, C., Kochanov, R. V., Tan, Y., Wcisło, P., Makhnev, V. Yu., Bernath, P. F., Birk, M., Boudon, V., Campargue, A., Coustenis, A., Drouin, B. J., Gamache, R. R., Hodges, J. T., Jacquemart, D., Mlawer, E. J., Nikitin, A. V., Perevalov, V. I., Rotger, M., Robert, S., Tennyson, J., Toon, G. C., Tran, H., Tyuterev, V. G., Adkins, E. M., Barbe, A., Bailey, D. M., Bielska, K., Bizzocchi, L., Blake, T. A., Bowesman, C. A., Cacciani, P., Čermák, P., Császár, A. G., Denis, L., Egbert, S. C., Egorov, O., Ermilov, A. Yu., Fleisher, A. J., Fleurbaey, H., Foltynowicz, A., Furtenbacher, T., Germann, M., Guest, E. R., Harrison, J. J., Hartmann, J.-M., Hjältén, A., Hu, S.-M., Huang, X., Johnson, T. J., Jóźwiak, H., Kassi, S., Khan, M. V., Kwabia-Tchana, F., Lee, T. J., Lisak, D., Liu, A.-W., Lyulin, O. M., Malarich, N. A., Manceron, L., Marinina, A. A., Massie, S. T., Mascio, J., Medvedev, E. S., Meshkov, V. V., Mellau, G. Ch., Melosso, M., Mikhailenko, S. N., Mondelain, D., Müller, H. S. P., O'Donnell, M., Owens, A., Perrin, A., Polyansky, O. L., Raston, P. L., Reed, Z. D., Rey, M., Richard, C., Rieker, G. B., Röske, C., Sharpe, S. W., Starikova, E., Stolarczyk, N., Stolyarov, A. V., Sung, K., Tamassia, F., Terragni, J., Ushakov, V. G., Vasilchenko, S., Vispoel, B., Vodopyanov, K. L., Wagner, G., Wójtewicz, S., Yurchenko, S. N., and Zobov, N. F.: The HITRAN2024 molecular spectroscopic database, J. Quant. Spectrosc. Radiat. Transf., 353, 109807, https://doi.org/10.1016/j.jqsrt.2026.109807, 2026.

Hillger, D., Kopp, T., Lee, T., Lindsey, D., Seaman, C., Miller, S., Solbrig, J., Kidder, S., Bachmeier, S., Jasmin, T., and Rink, T.: First-Light Imagery from Suomi NPP VIIRS, Bull. Am. Meteorol. Soc., 94, 1019–1029, https://doi.org/10.1175/BAMS-D-12-00097.1, 2013.

Hu, H., Landgraf, J., Detmers, R., Borsdorff, T., Aan De Brugh, J., Aben, I., Butz, A., and Hasekamp, O.: Toward Global Mapping of Methane With TROPOMI: First Results and Intersatellite Comparison to GOSAT, Geophys. Res. Lett., 45, 3682–3689, https://doi.org/10.1002/2018GL077259, 2018.

Irakulis-Loitxate, I., Guanter, L., Maasakkers, J. D., Zavala-Araiza, D., and Aben, I.: Satellites Detect Abatable Super-Emissions in One of the World's Largest Methane Hotspot Regions, Environ. Sci. Technol., 56, 2143–2152, https://doi.org/10.1021/acs.est.1c04873, 2022.

Jacob, D. J., Turner, A. J., Maasakkers, J. D., Sheng, J., Sun, K., Liu, X., Chance, K., Aben, I., McKeever, J., and Frankenberg, C.: Satellite observations of atmospheric methane and their value for quantifying methane emissions, Atmos. Chem. Phys., 16, 14371–14396, https://doi.org/10.5194/acp-16-14371-2016, 2016.

Jongaramrungruang, S., Matheou, G., Thorpe, A. K., Zeng, Z.-C., and Frankenberg, C.: Remote sensing of methane plumes: instrument tradeoff analysis for detecting and quantifying local sources at global scale, Atmos. Meas. Tech., 14, 7999–8017, https://doi.org/10.5194/amt-14-7999-2021, 2021.

Lechevallier, L., Vasilchenko, S., Grilli, R., Mondelain, D., Romanini, D., and Campargue, A.: The water vapour self-continuum absorption in the infrared atmospheric windows: new laser measurements near 3.3 and 2.0 µm, Atmos. Meas. Tech., 11, 2159–2171, https://doi.org/10.5194/amt-11-2159-2018, 2018.

Lin, G., Wolfe, R. E., Zhang, P., Dellomo, J. J., and Tan, B.: Ten Years of VIIRS On-Orbit Geolocation Calibration and Performance, Remote Sens., 14, 4212, https://doi.org/10.3390/rs14174212, 2022.

Lorente, A., Borsdorff, T., Butz, A., Hasekamp, O., aan de Brugh, J., Schneider, A., Wu, L., Hase, F., Kivi, R., Wunch, D., Pollard, D. F., Shiomi, K., Deutscher, N. M., Velazco, V. A., Roehl, C. M., Wennberg, P. O., Warneke, T., and Landgraf, J.: Methane retrieved from TROPOMI: improvement of the data product and validation of the first 2 years of measurements, Atmos. Meas. Tech., 14, 665–684, https://doi.org/10.5194/amt-14-665-2021, 2021.

Menzel, P.: Applications with Meteorological Satellites, SAT, 1078, NOAA/NESDIS, https://library.wmo.int/fr/records/item/37305-applications-with-meteorological-satellites (last access: 14 March 2026), 2001.

Neinavaz, E., Schlerf, M., Darvishzadeh, R., Gerhards, M., and Skidmore, A. K.: Thermal infrared remote sensing of vegetation: Current status and perspectives, Int. J. Appl. Earth Obs. Geoinf., 102, 102415, https://doi.org/10.1016/j.jag.2021.102415, 2021.

Ni, Q., Zhou, M., Wang, J., Wang, T., Wang, G., and Wang, P.: Intercomparison of CH_4 Products in China from GOSAT, TROPOMI, IASI, and AIRS Satellites, Remote Sens., 15, 4499, https://doi.org/10.3390/rs15184499, 2023.

Panditharatne, S., Cox, C., Song, R., Siddans, R., Bantges, R., Murray, J., Fox, S., Fox, C., and Brindley, H.: Exploiting airborne far-infrared measurements to optimise an ice cloud retrieval, Atmos. Chem. Phys., 25, 9981–9998, https://doi.org/10.5194/acp-25-9981-2025, 2025.

Roger, J., Guanter, L., Gorroño, J., and Irakulis-Loitxate, I.: Exploiting the entire near-infrared spectral range to improve the detection of methane plumes with high-resolution imaging spectrometers, Atmos. Meas. Tech., 17, 1333–1346, https://doi.org/10.5194/amt-17-1333-2024, 2024.

Scafutto, R. D. P. M. and De Souza Filho, C. R.: Detection of Methane Plumes Using Airborne Midwave Infrared (3–5 µm) Hyperspectral Data, Remote Sens., 10, 1237, https://doi.org/10.3390/rs10081237, 2018.

Siddans, R., Knappett, D., Kerridge, B., Waterfall, A., Hurley, J., Latter, B., Boesch, H., and Parker, R.: Global height-resolved methane retrievals from the Infrared Atmospheric Sounding Interferometer (IASI) on MetOp, Atmos. Meas. Tech., 10, 4135–4164, https://doi.org/10.5194/amt-10-4135-2017, 2017.

Simpson, I. R., McKinnon, K. A., Kennedy, D., Lawrence, D. M., Lehner, F., and Seager, R.: Observed humidity trends in dry regions contradict climate models, Proc. Natl. Acad. Sci. U.S.A., 121, e2302480120, https://doi.org/10.1073/pnas.2302480120, 2024.

Sinfrared, R. V. and Zimmermann, T.: MWIR for Remote Sniffing and Locating of Gases, Photonics Spectra, https://www.photonics.com/Articles/MWIR-for-Remote-Sniffing-and-Locating-of-Gases/a56861 (last access: 17 May 2026), 2014.

Tran, D. A., Vilà-Guerau de Arellano, J., Luijkx, I. T., Gerbig, C., Gałkowski, M., Botía, S., Faassen, K., and Zaehle, S.: Increasing diurnal and seasonal amplitude of atmospheric methane mole fraction in Central Siberia between 2010–2021, Atmos. Chem. Phys., 25, 16553–16588, https://doi.org/10.5194/acp-25-16553-2025, 2025.

US Environmental Protection Agency: Extension of Deadlines in Standards of Performance for New, Reconstructed, and Modified Sources and Emissions Guidelines for Existing Sources: Oil and Natural Gas Sector Climate Review, https://www.federalregister.gov/documents/ (last access: 23 May 2026), 2025.

Vihma, T., Pirazzini, R., Fer, I., Renfrew, I. A., Sedlar, J., Tjernström, M., Lüpkes, C., Nygård, T., Notz, D., Weiss, J., Marsan, D., Cheng, B., Birnbaum, G., Gerland, S., Chechin, D., and Gascard, J. C.: Advances in understanding and parameterization of small-scale physical processes in the marine Arctic climate system: a review, Atmos. Chem. Phys., 14, 9403–9450, https://doi.org/10.5194/acp-14-9403-2014, 2014.

Wang, W., Cao, C., and Blonski, S.: NOAA-21 VIIRS Thermal Emissive Bands Early On-Orbit Calibration Performance and Improvements, IEEE Trans. Geosci. Remote Sens., 62, 1–13, https://doi.org/10.1109/TGRS.2024.3458869, 2024.

Webber, C. M. and Kerekes, J. P.: An examination of enhanced atmospheric methane detection methods for predicting performance of a novel multiband uncooled radiometer imager, Atmos. Meas. Tech., 13, 5359–5367, https://doi.org/10.5194/amt-13-5359-2020, 2020.

Worden, J., Green, P., Eldering, A., and Sherwin, E.: Common practices for quantifying methane emissions from plumes detected by remote sensing, NIST IR 8575, National Institute of Standards and Technology (US), Gaithersburg, MD, https://doi.org/10.6028/NIST.IR.8575, 2025.

Xiong, X., Barnet, C., Maddy, E., Sweeney, C., Liu, X., Zhou, L., and Goldberg, M.: Characterization and validation of methane products from the Atmospheric Infrared Sounder (AIRS), J. Geophys. Res., 113, 2007JG000500, https://doi.org/10.1029/2007JG000500, 2008.

Xu, S., Wang, X., Sun, Q., and Dong, K.: MWIRGas-YOLO: Gas Leakage Detection Based on Mid-Wave Infrared Imaging, Sensors, 24, 4345, https://doi.org/10.3390/s24134345, 2024.

Zheng, B., Cohen, J. B., Lu, L., Hu, W., Tiwari, P., Lolli, S., Garzelli, A., Su, H., and Qin, K.: How can we trust TROPOMI based methane emissions estimation: calculating emissions over unidentified source regions, Atmos. Chem. Phys., 26, 1931–1946, https://doi.org/10.5194/acp-26-1931-2026, 2026.

Zhizhin, M., Elvidge, C., and Poyda, A.: Night-Time Detection of Subpixel Emitters with VIIRS Mid-Wave Infrared Bands M12–M13, Remote Sens., 15, 1189, https://doi.org/10.3390/rs15051189, 2023.

Zhou, L., Warner, J., Nalli, N. R., Wei, Z., Oh, Y., Bruhwiler, L., Liu, X., Divakarla, M., Pryor, K., Kalluri, S., and Goldberg, M. D.: Spatiotemporal Variability of Global Atmospheric Methane Observed from Two Decades of Satellite Hyperspectral Infrared Sounders, Remote Sens., 15, 2992, https://doi.org/10.3390/rs15122992, 2023.

Zhou, R., Di, D., Li, J., and Li, Z.: Enhanced Moisture Retrieval Near Boundary Layer From Satellite Sounder Data Through Atmospheric-Surface Radiance Separation, Geophys. Res. Lett., 52, e2024GL113404, https://doi.org/10.1029/2024GL113404, 2025.